CEERS Key Paper. VII. JWST/MIRI Reveals a Faint Population of Galaxies at Cosmic Noon Unseen by Spitzer

Kirkpatrick, Allison; Yang, Guang; Le Bail, Aurélien; Troiani, Greg; Bell, Eric F.; Cleri, Nikko J.; Elbaz, David; Finkelstein, Steven L.; Hathi, Nimish P.; Hirschmann, Michaela

[Link to publication in University of Groningen/UMCG research database](#)

CrossMark

CEERS Key Paper. VII. JWST/MIRI Reveals a Faint Population of Galaxies at Cosmic Noon Unseen by Spitzer

Allison Kirkpatrick[1], Guang Yang[2,3], Aurélien Le Bail[4], Greg Troiani[1], Eric F. Bell[5], Nikko J. Cleri[6,7], David Elbaz[4], Steven L. Finkelstein[8], Nimish P. Hathi[9], Michaela Hirschmann[10], Benne W. Holwerda[11], Dale D. Kocevski[12], Ray A. Lucas[13], Jed McKinney[14], Casey Papovich[6,7], Pablo G. Pérez-González[15], Alexander de la Vega[16], Micaela B. Bagley[8], Emanuele Daddi[4], Mark Dickinson[17], Henry C. Ferguson[9], Adriano Fontana[18], Andrea Grazian[19], Norman A. Grogin[9], Pablo Arrabal Haro[17], Jeyhan S. Kartaltepe[20], Lisa J. Kewley[21], Anton M. Koekemoer[13], Jennifer M. Lotz[22], Laura Pentericci[18], Nor Pirzkal[23], Swara Ravindranath[13], Rachel S. Somerville[24], Jonathan R. Trump[25], Stephen M. Wilkins[26,27], and L. Y. Aaron. Yung[28,29]

[1] Department of Physics and Astronomy, University of Kansas, Lawrence, KS 66045, USA
[2] Kapteyn Astronomical Institute, University of Groningen, P.O. Box 800, 9700 AV Groningen, The Netherlands
[3] SRON Netherlands Institute for Space Research, Postbus 800, 9700 AV Groningen, The Netherlands
[4] Université Paris-Saclay, Université Paris Cité, CEA, CNRS, AIM, F-91191, Gif-sur-Yvette, France
[5] Department of Astronomy, University of Michigan, 1085 South University Avenue, Ann Arbor, MI 48109-1107, USA
[6] Department of Physics and Astronomy, Texas A&M University, College Station, TX 77843-4242, USA
[7] George P. and Cynthia Woods Mitchell Institute for Fundamental Physics and Astronomy, Texas A&M University, College Station, TX 77843-4242, USA
[8] Department of Astronomy, The University of Texas at Austin, Austin, TX, USA
[9] Space Telescope Science Institute, Baltimore, MD, USA
[10] Institute of Physics, Laboratory of Galaxy Evolution, Ecole Polytechnique Fédérale de Lausanne (EPFL), Observatoire de Sauverny, 1290 Versoix, Switzerland
[11] Physics & Astronomy Department, University of Louisville, Louisville, KY 40292, USA
[12] Department of Physics and Astronomy, Colby College, Waterville, ME 04901, USA
[13] Space Telescope Science Institute, 3700 San Martin Drive, Baltimore, MD 21218, USA
[14] Department of Astronomy, The University of Texas at Austin, 2515 Speedway, Austin, TX 78712, USA
[15] Centro de Astrobiología (CAB), CSIC-INTA, Ctra. de Ajalvir km 4, Torrejón de Ardoz, E-28850, Madrid, Spain
[16] Department of Physics and Astronomy, University of California, 900 University Avenue, Riverside, CA 92521, USA
[17] NSF's National Optical-Infrared Astronomy Research Laboratory, 950 North Cherry Avenue, Tucson, AZ 85719, USA
[18] INAF—Osservatorio Astronomico di Roma, via di Frascati 33, I-00078 Monte Porzio Catone, Italy
[19] INAF–Osservatorio Astronomico di Padova, Vicolo dell'Osservatorio 5, I-35122, Padova, Italy
[20] Laboratory for Multiwavelength Astrophysics, School of Physics and Astronomy, Rochester Institute of Technology, 84 Lomb Memorial Drive, Rochester, NY 14623, USA
[21] Center for Astrophysics | Harvard & Smithsonian, 60 Garden Street, Cambridge, MA 02138, USA
[22] Gemini Observatory/NSF's National Optical-Infrared Astronomy Research Laboratory, 950 North Cherry Avenue, Tucson, AZ 85719, USA
[23] ESA/AURA Space Telescope Science Institute
[24] Center for Computational Astrophysics, Flatiron Institute, 162 5th Avenue, New York, NY 10010, USA
[25] Department of Physics, 196 Auditorium Road, Unit 3046, University of Connecticut, Storrs, CT 06269, USA
[26] Astronomy Centre, University of Sussex, Falmer, Brighton BN1 9QH, UK
[27] Institute of Space Sciences and Astronomy, University of Malta, Msida MSD 2080, Malta
[28] Astrophysics Science Division, NASA Goddard Space Flight Center, 8800 Greenbelt Road, Greenbelt, MD 20771, USA

Abstract

The Cosmic Evolution Early Release Science program observed the Extended Groth Strip (EGS) with the Mid-Infrared Instrument (MIRI) on the James Webb Space Telescope (JWST) in 2022. In this paper, we discuss the four MIRI pointings that observed with longer-wavelength filters, including F770W, F1000W, F1280W, F1500W, F1800W, and F2100W. We compare the MIRI galaxies with the Spitzer/MIPS 24 μm population in the EGS field. We find that MIRI can observe an order of magnitude deeper than MIPS in significantly shorter integration times, attributable to JWST's much larger aperture and MIRI's improved sensitivity. MIRI is exceptionally good at finding faint ($L_{IR} < 10^{10} L_{\odot}$) galaxies at $z \sim 1$–2. We find that a significant portion of MIRI galaxies are "mid-IR weak"—they have strong near-IR emission and relatively weaker mid-IR emission, and most of the star formation is unobscured. We present new IR templates that capture how the mid-to-near-IR emission changes with increasing infrared luminosity. We present two color–color diagrams to separate mid-IR weak galaxies and active galactic nuclei (AGN) from dusty star-forming galaxies and find that these color diagrams are most effective when used in conjunction with each other. We present the first number counts of 10 μm sources and find that there are $\lesssim$10 IR AGN per MIRI pointing, possibly due to the difficulty of distinguishing AGN from intrinsically mid-IR weak galaxies (due to low metallicities or dust content). We conclude that MIRI is most effective at observing moderate-luminosity ($L_{IR} = 10^9$–$10^{10} L_{\odot}$) galaxies at $z = 1$–2, and that photometry alone is not effective at identifying AGN within this faint population.

---

[29] NASA Postdoctoral Fellow.

1. Introduction

In the past two decades, the Multi-Band Imaging Photometer (MIPS) on the Spitzer Space Telescope revealed a new understanding of the infrared Universe through observations of a previously undetected population of infrared-luminous galaxies at $z > 0.5$ (Chary et al. 2004; Papovich et al. 2004). MIPS observations demonstrated that the bulk of star formation in the Universe occurred when the Universe was a mere 3–6 billion yr old ($z \sim 1$–2), the so-called "cosmic noon" epoch (Pérez-González et al. 2005; Caputi et al. 2007). Furthermore, contrary to the local Universe, this star formation occurred predominantly in dust-rich galaxies, namely, (ultra)luminous infrared galaxies ((U)LIRGs, $L_{IR} > 10^{11} L_\odot$, where L_{IR} is the integrated luminosity from 8 to 1000 μm; Magnelli et al. 2011). Although such galaxies exist today, they contribute relatively little to the local star formation rate (SFR; Rodighiero et al. 2010).

While (U)LIRGs at cosmic noon are forming stars at prodigious rates (SFRs of 100–1000 $M_\odot$ yr^{-1}), they predominately lie on the main sequence of star formation, in stark contrast to local (U)LIRGs (Elbaz et al. 2011; Kartaltepe et al. 2012). The main sequence is an empirical tight correlation between the SFR and stellar masses (M_*) of galaxies (Elbaz et al. 2007; Noeske et al. 2007). Galaxies on the main sequence are presumed to be undergoing long-lived secular evolution, while galaxies above the main sequence are undergoing short bursts of star formation, likely triggered by a major merger event. The Infrared Spectrograph (IRS) instrument on Spitzer was used to probe the mid-IR emission of these cosmic noon (U)LIRGs in detail and found that their mid-IR dust emission is remarkably similar to that of isolated LIRGs in the local Universe, indicating a metal-enriched environment and the distinct lack of an obscured nuclear starburst (Kirkpatrick et al. 2012, 2015; Sajina et al. 2012; Pope et al. 2013; McKinney et al. 2020). Simply put, dusty star-forming galaxies in the distant Universe resemble scaled-up versions of nonmerging star-forming galaxies in the local Universe.

All massive galaxies are presumed to host a supermassive black hole at their centers. The peak of the supermassive black hole accretion rate density also occurs at cosmic noon (Delvecchio et al. 2014; Peca et al. 2023), making this epoch of fundamental importance to understanding the concurrent buildup of stellar and black hole mass. Furthermore, there is evidence from both deep X-ray and IR observations that the bulk of black hole growth at cosmic noon is obscured (Del Moro et al. 2016; Ananna et al. 2019; Yang et al. 2023a). Mid-IR emission can reliably be used to identify both obscured and unobscured active galactic nuclei (AGN; Padovani et al. 2017; Yang et al. 2023a). In previous mid-IR surveys with Spitzer/MIPS or the Wide-Field Survey Infrared Explorer, AGN make up at least 15% of extragalactic sources with $S_{24} > 100$ μJy (Jarrett et al. 2011; Kirkpatrick et al. 2017a, hereafter K17).

In star-forming galaxies, the mid-IR emission is dominated by polycyclic aromatic hydrocarbon (PAH) complexes at 6.2, 7.7, 11.2, and 12.7 μm. AGN typically have a dusty toroidal structure surrounding the accretion disk that radiates as a power law in the mid-IR. These differences make the mid-IR advantageous for identifying populations of star-forming galaxies and AGN, and several color–color methods exist for

doing so (Lacy et al. 2004; Stern et al. 2005; Donley et al. 2012; Messias et al. 2012; Kirkpatrick et al. 2013). The Mid-Infrared Instrument (MIRI; Rieke et al. 2015) on the James Webb Space Telescope (JWST; Gardner et al. 2006) has several improvements over MIPS; the greatly improved spatial resolution allows for dramatically improved source deblending, and the MIRI filter set better spans the mid-IR emission. These improvements led to studies predicting that MIRI would be efficient and reliable at finding AGN (Messias et al. 2012; Langeroodi & Hjorth 2023) at high redshift ($z > 5$; Volonteri et al. 2017) or at lower luminosities and high obscuration levels (K17; Yang et al. 2021).

In this paper, we explore the nature of the sources in one of the first MIRI surveys, which was observed as part of the Cosmic Evolution Early Release Science (CEERS; PI: S. Finkelstein) program. In Section 2, we discuss the observations. In Section 3, we compare the MIRI sources to the MIPS sources in the Extended Groth Strip (EGS) field, and we discuss the presence of AGN. We discuss the implications of the MIRI observations, including the surprising lack of AGN, in Section 4. Finally, we present our conclusions in Section 5.

In this work, we assume a standard flat cosmology with $H_0 = 70$ Mpc km^{-1} s^{-1}, $\Omega_M = 0.3$, and $\Lambda = 0.7$.

2. Data

2.1. MIRI Observations

The CEERS MIRI observations, data reduction, and photometric catalogs are fully described in Yang et al. (2023a); here, we summarize the relevant details. The EGS field was observed with eight MIRI pointings. Four "blue" pointings were only observed in the F560W and F770W filters. In this paper, we discuss the four "red" pointings, observed in the longer-wavelength filters (Table 1). Pointings 1 (Figure 1) and 2 were observed in 2022 July, while pointings 5 and 8 were observed in 2022 December. Pointings 1 and 2 do not overlap with CEERS NIRCam observations. The F770W and F2100W filters are only observed in pointings 1 and 2. Table 1 lists the effective wavelength (λ_{eff}) and the 5σ flux limits for each filter in each pointing (Yang et al. 2023b). The MIRI field of view (FOV) is $112\rlap{.}''6 \times 73\rlap{.}''5$, bringing the total observed area to 9.2 arcmin^2 for the four MIRI pointings discussed in this work.

The MIRI photometry was extracted with T-PHOT (Merlin et al. 2015) using Hubble Space Telescope (HST) F160W observations as a prior. HST positions were used rather than NIRCam due to the lack of uniform NIRCam coverage in the MIRI pointings. For details of the MIRI observations, data reduction, photometry extraction, and quality assessment, see Yang et al. (2021), Papovich et al. (2023), and the CEERS MIRI observation paper (Yang et al. 2023b).

The use of near-IR HST priors resulted in some spurious detections, where a galaxy is visible in the HST image but not in all of the MIRI filters. To be included in the final sample, we required sources to (1) have a signal-to-noise ratio (S/N) of >3 in at least two MIRI bands and (2) be well fit by a mid-IR template (see Sections 2.4 and 3.2 for a full description of the template fitting procedure). There are 911 sources with S/N > 3 in at least one MIRI band. Of these, there are 575 (466) that have S/N > 3 in at least two (three) bands. From the parent sample of 575 sources, 482 were well fit by mid-IR

Table 1
CEERS Red MIRI Pointings

Pointing[a]	R.A. (J2000)	Decl. (J2000)	Filter	λ_{eff} (μm)	Exp. Time (s)	5σ Depth[b] (μJy)
1	14:20:38.88	+53:03:04.6	770W	7.7	1648	0.21
			1000W	10.0	1673	0.42
			1280W	12.8	1673	0.78
			1500W	15.0	1673	1.27
			1800W	18.0	1698	2.51
			2100W	21.0	4812	4.79
2	14:20:17.42	+52:59:16.2	770W	7.7	1648	0.21
			1000W	10.0	1673	0.43
			1280W	12.8	1673	0.82
			1500W	15.0	1673	1.15
			1800W	18.0	1698	2.73
			2100W	21.0	4812	3.87
5	14:19:03.74	+52:49:08.5	1000W	10.0	1243	0.50
			1280W	12.8	932	1.27
			1500W	15.0	932	2.31
			1800W	18.0	1243	3.98
8	14:19:21.78	+52:48:55.5	1000W	10.0	1243	0.47
			1280W	12.8	932	1.32
			1500W	15.0	932	2.00
			1800W	18.0	1243	3.98

Notes.
[a] For the layout of the pointings, see https://ceers.github.io/obs.html.
[b] Flux limit calculations are derived from the AB magnitude limits presented in Yang et al. (2023b).

templates and are included in the final sample. The remaining 93 sources have faint fluxes (<1 μJy) in the mid-IR ($\lambda > 5$ μm) and no unambiguous PAH features.

2.2. Redshifts

We cross-match our MIRI sources with the CANDELS (Grogin et al. 2011; Koekemoer et al. 2011) EGS catalog of Finkelstein et al. (2022), which includes HST/ACS+WFC3 and Spitzer/IRAC photometry and photometric redshifts derived with the EAZY code (Brammer et al. 2008), fitting a suite of templates to the HST+IRAC photometry. The code produces a redshift posterior probability distribution that includes the 68% confidence intervals. The final redshift is the peak of the probability distribution. As discussed below, for some MIRI sources, we use photometric redshifts from the CANDELS catalog of Stefanon et al. (2017), measured by fitting HST and IRAC data with various different codes. The z_{phot} is the median redshift determined through five separate codes that fit templates to the UV/optical/near-IR data. A mere 20 sources have spectroscopic redshifts, and we use these where available.

Optical photometric redshifts can carry a degree of uncertainty if the templates are not representative of the full galaxy population or the photometry is noisy or sparse (Newman & Gruen 2022). MIRI covers the PAH features for the majority of our galaxies, which may provide additional constraints on the redshifts due to their prominence (Pope et al. 2008; Kirkpatrick et al. 2012). MIRI is the first instrument with closely spaced filters allowing for the identification of PAH features with photometry alone.

To test how well fitting templates to mid-IR data can reproduce optical redshifts, we fit all galaxies with three templates described in more detail in Section 2.4. Two templates are a star-forming template ("MIR0.3") and an

AGN template ("MIR0.7") from the Kirkpatrick et al. (2015, hereafter K15) library. The third template is the $L_{\mathrm{IR}} = 10^{10} L_\odot$ template from the Chary & Elbaz (2001, hereafter CE01) library. We include the IRAC 4.5 and 5.8 μm photometric points, along with all available MIRI data, in the fitting, as these are useful in identifying the stellar bump at $\lambda \sim 1.6$ μm and the stellar minimum at $\lambda \sim 5$ μm. For all but 32 sources, the MIRI redshift agrees with the optical redshift from Finkelstein et al. (2022) within the confidence interval on the optical redshift. We therefore adopt the Finkelstein et al. (2022) redshifts for these galaxies. Of the 32 sources where the two redshifts do not agree, the MIRI redshifts of 24 sources agree with the optical redshifts from Stefanon et al. (2017) within the confidence interval on the optical redshift. We adopt the Stefanon et al. (2017) redshifts for these sources. For the remaining eight sources, we visually compare the photometry with a star-forming template at the MIRI and optical redshifts, and we determine that the MIRI redshift provides the best fit to the PAH features. We therefore adopt the MIRI redshifts.

2.3. MIPS 24 µm Observations

The EGS field was observed with Spitzer/MIPS as part of the Spitzer/FIDEL Legacy project (PI: M. Dickinson; Magnelli et al. 2009; FIDEL Team 2020). The typical MIPS exposure time per position within the CANDELS/CEERS areas is 14,000 s, and the MIPS data analyzed here cover the CANDELS WFC3 field of $\sim$200 arcmin^2, nearly 20$\times$ larger than the CEERS MIRI area. The MIPS beam size is 6″, causing blending of closely spaced sources within each beam, which have been carefully deblended based on HST and IRAC prior positions and fluxes. Photometry has been calculated with a point spread function fitting method to extract MIPS fluxes at the positions of the HST/F160W priors from the catalog of Stefanon et al. (2017). The methodology is similar to what is
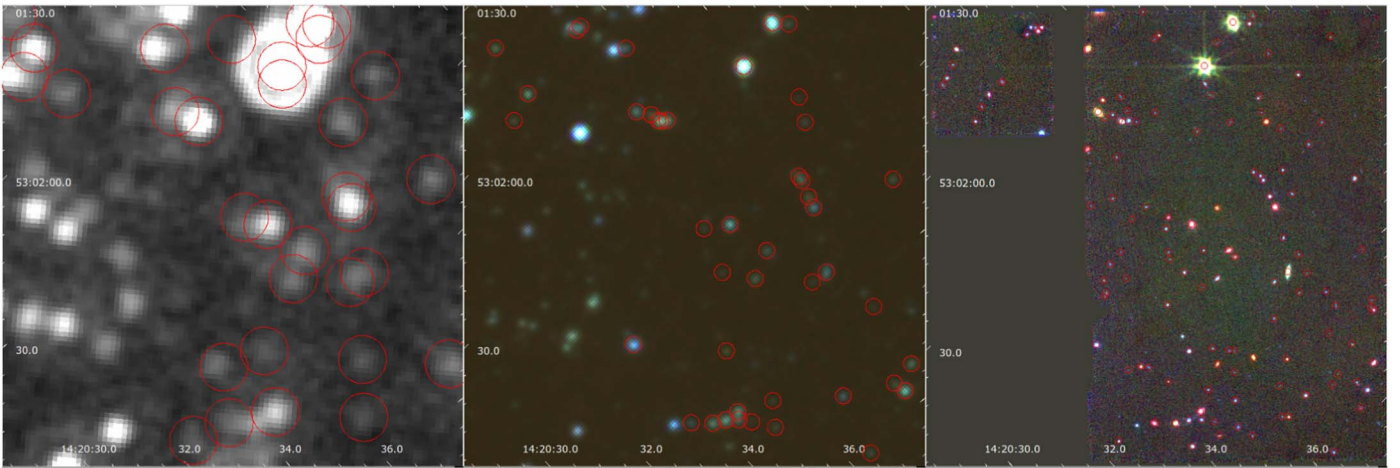
Figure 1. We show MIRI pointing 1 (right panel) alongside the Spitzer/IRAC (middle) and MIPS (left) observations of the same region. The apertures show the location of detected sources in each image (MIRI region only). For the MIPS (IRAC) image, the apertures are $6''(2'')$, corresponding to the instrument beam size. In the IRAC image, blue corresponds to channel 1 (3.6 μm), green corresponds to channel 2 (4.5 μm), and red corresponds to channel 3 (5.8 μm). In the MIRI image, the 770W filter is blue, F1000W is green, and F1280W is red.

described in Jin et al. (2018) and Liu et al. (2018), and full details will be provided in a forthcoming paper (Le Bail et al. 2023, in preparation). Flux biases and uncertainties were measured using extensive simulations. There are $\sim$4000 MIPS sources with $S_{24} > 21$ μJy, which is the average 3σ flux limit in the Le Bail catalog. Figure 1 illustrates the image quality of MIRI compared with IRAC and MIPS. With MIPS, the larger angular resolution leads to multiple galaxies falling within one beam. MIRI observations alleviate this challenge, enabling the detection of fainter, nonisolated sources.

2.4. Infrared Templates

To measure redshifts, estimate L_{IR}, and search for AGN emission, we fit a suite of templates to the MIRI population (Section 3.2). These templates are the K15 MIR and CE01 libraries. We opt for this method because it is less computationally expensive than codes such as CIGALE. The K15 and CE01 templates are empirically derived from infrared observations of galaxies, while CIGALE and other spectral energy distribution (SED) fitters produce model spectra using stellar population synthesis, dust emission models, radiative transfer calculations, or energy balance requirements.

The K15 templates were empirically created from 343 24 μm–selected galaxies spanning the redshift range $z \sim 0.5$–3.0. Every galaxy had a Spitzer/IRS spectrum (low-resolution spectroscopy) that was modeled by combining a PAH template with power-law emission attributed to a torus. This spectral modeling determined $f(\text{AGN})_{MIR}$, which is the fraction of mid-IR emission attributable to the power-law component. $f(\text{AGN})_{MIR}$ spans the range 0.0–1.0 (fully star-forming to fully AGN). Additionally, all galaxies had JHK, Spitzer/IRAC, and Herschel/PACS and SPIRE photometry covering the full IR wavelength range.

Galaxies were sorted by $f(\text{AGN})_{MIR}$ in increments of 0.1 (that is, the pure star-forming bin would have galaxies with $0 \leqslant f(\text{AGN})_{MIR} < 0.1$, while the pure AGN bin would have $0.9 \leqslant f(\text{AGN})_{MIR} \leqslant 1.0$; every other bin contains galaxies with $f(\text{AGN})_{MIR}$ indicating varying mixes of star formation and AGN emission) to create empirical templates. From $\lambda = 0.9$ to 20 μm, the normalized photometry and spectroscopy

were averaged together as a function of wavelength using a bootstrapping technique. Beyond 20 μm, the normalized photometry was fit with a two-temperature modified blackbody.

Crucially, all galaxies in the sample used to create the K15 template library have $L_{IR} > 10^{11}$ $L_{\odot}$. They are representative of the (U)LIRG population at cosmic noon.

As discussed below, lower-luminosity templates are also needed to represent the MIRI population. To this end, we included the CE01 templates with $L_{IR} = [2 \times 10^8, 5 \times 10^8, 1 \times 10^9, 5 \times 10^9, 1 \times 10^{10}, 5 \times 10^{10}]$ $L_{\odot}$ in our fitting procedure.

CE01 used models tailored to match the ultraviolet–submillimeter SED of four galaxy prototypes: Arp 220, NGC 6090, M82, and M51. These four representative models were then divided into mid-infrared (4–20 μm) and far-infrared (20–1000 μm) components and fit to the ISOCAM and IRAS observations of local galaxies and (U)LIRGs in the IRAS Bright Galaxy Survey. Galaxies were sorted into luminosity bins, and the best-fitting mid- and far-infrared models were averaged together to yield the final representative template SED for each luminosity bin.

3. Results

3.1. Comparison with Spitzer 24 μm

Prior to the launch of JWST, Spitzer was the premier mid-IR observatory. To better understand the new mid-IR Universe revealed through MIRI observations, we compare the properties of the CEERS JWST/MIRI galaxies (traced through the 18 μm population) to the EGS Spitzer/MIPS population.

Figure 2 compares the luminosity and redshift distribution of the full EGS MIPS population and the 18 μm population. We choose to show the 18 μm population, as 18 μm is close in wavelength to 24 μm, F1800W was observed in all four pointings, and the F1800W sensitivity is better than that at F2100W. There are 433 sources with S/N $\geqslant$ 3 in the F1800W filter.

As seen in the top panel, MIPS sources have a bimodal redshift distribution with peaks at $z \sim 1$ and 2 due to PAH emission. At $z \sim 1$, the 11.2 and 12.7 μm PAH complexes fall within the 24 μm bandpass, and at $z \sim 2$, the 7.7 μm PAH
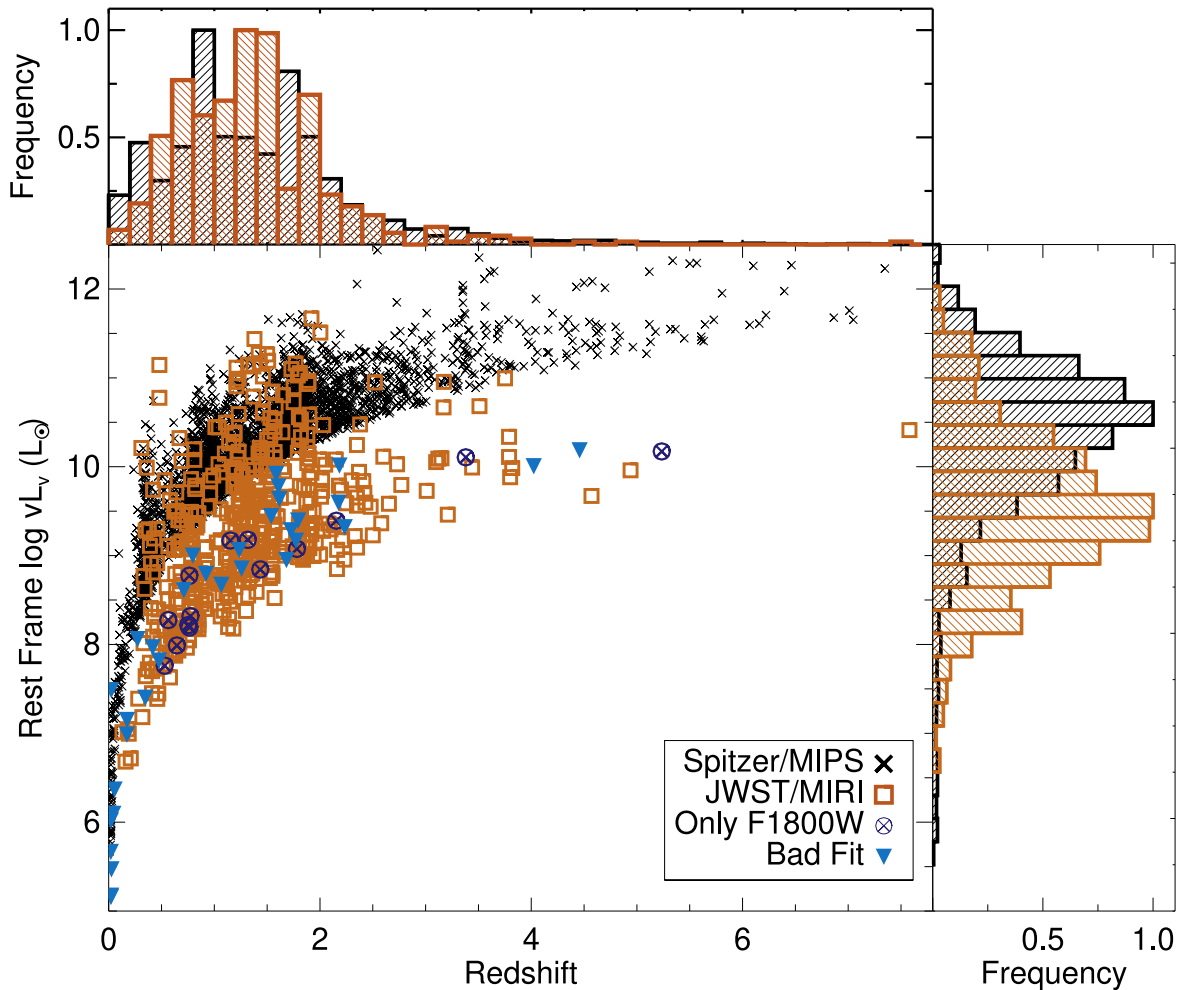
Figure 2. Redshift vs. νL_ν for the full MIPS population ($\nu = 24$ μm; black crosses) and the MIRI population ($\nu = 18$ μm; orange squares). The surprising lack of high-z MIRI sources is attributable to the lack of bright dust features at $\lambda_{\rm rest} \leqslant 5\mu$m and the much smaller survey area. MIRI is capable of detecting fainter sources than MIPS at all redshifts in a fraction of the time. We show the final sample (S/N > 3 in at least two bands and well fit by a mid-IR template; 385 18 μm galaxies meet these criteria) in orange. We also show the sources that have S/N > 3 in only the F1800W filter (14 sources; blue circles with crosses) and the sources that are not well fit with a mid-IR template (34 sources; blue triangles). Our selection criteria are not biasing the final sample toward brighter sources. The histograms in the side panels have been arbitrarily normalized due to the stark difference in the number of sources.

feature slides in. Additionally, the 9.7 μm silicate absorption feature falls in the bandpass at $z \sim 1.5$, contributing to the dearth of detections. The 18 μm distribution also has noticeable peaks where different PAH features slide into the filter. The peak around $z \sim 0.5$ is attributable to the 11.2 and 12.7 μm features. The majority of 18 μm sources lie around $z \sim 1.3$. This is due to the 7.7 μm complex falling in the F1800W bandpass at $z = 1.3$. The 7.7 μm complex is the broadest of the PAH features, spanning $\lambda = 7.2$–8.2 μm. This rest wavelength range will cause a brightening at $\lambda_{\rm obs} = 18$ μm from $z = 1.2$ to 1.5. The 6.2 μm PAH feature falls in the F1800W bandpass at $z = 1.9$, also visible in the redshift distribution.

The redshift distributions are most instructive when considered alongside the νL_ν distributions. Here, νL_ν refers to the rest-frame photometry in either the 24 μm or F1800W filter. MIRI galaxies are an order of magnitude less luminous in the infrared at all redshifts, which can be attributed to the increased sensitivity. It is interesting, and perhaps unexpected, to note the lack of MIRI detections of bright sources at $z > 3$. At $z > 3$, F1800W probes the faintest dust emission ($\lambda \lesssim 5$ μm), contributing to the lack of high-redshift sources. In terms of numbers of high-z sources, MIPS has the advantage of a much

larger FOV than MIRI ($12\times$ greater). Uncovering a high-redshift population of dusty galaxies will require a large-area MIRI survey with the longest-wavelength filters in order to probe the dust emission at higher redshifts.

The 18 μm population has a very similar luminosity and redshift distribution as the 21 μm population. There are 121 sources in pointings 1 and 2 detected with MIPS and 264 sources detected in MIRI F2100W. The 21 μm MIRI distribution peaks at more than an order of magnitude lower flux than the MIPS distribution, attributable to the improved sensitivities of JWST compared with Spitzer, largely due to the nearly $8\times$ increase in diameter. F1800W reaches fainter flux limits than F2100W in similar exposure times, but F2100W can trace dust emission out to higher redshifts.

Figure 2 highlights MIRI's strengths: low-luminosity galaxies at cosmic noon ($z = 1$–2). Here, MIRI probes a population inaccessible from Spitzer, and it does it in less than an hour. The lack of filters at $\lambda > 21$ μm means that the brightest dust emission, the PAH features, are no longer detectable at $z > 2$. This makes MIRI ideally suited for detecting galaxies well below the knee of the luminosity function at cosmic noon.
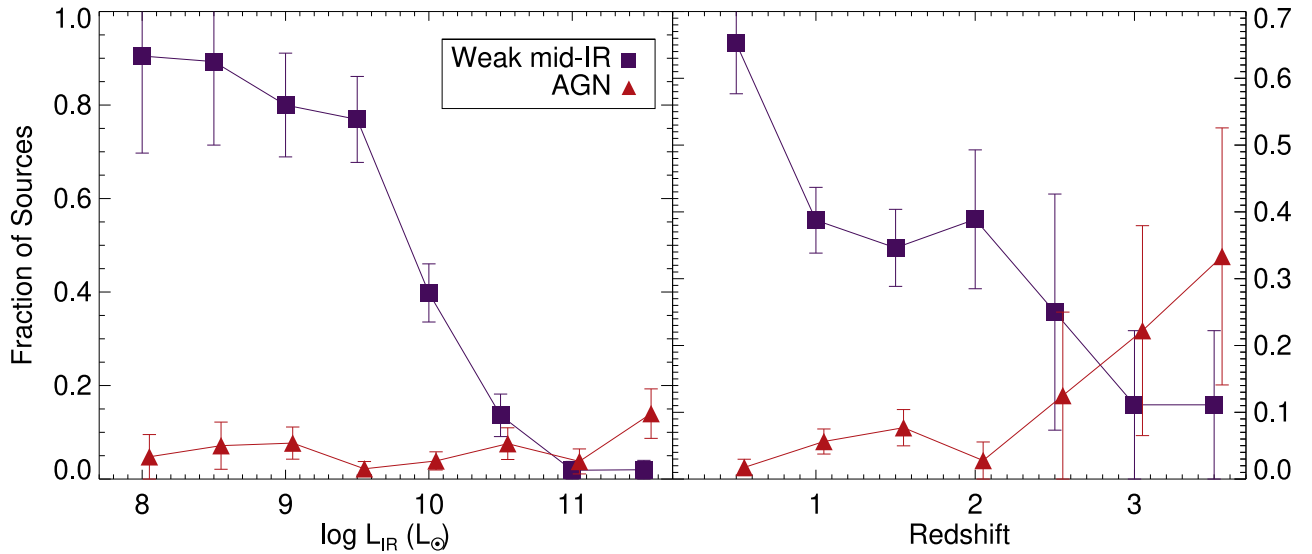
Figure 3. The fraction of galaxies that are mid-IR weak (i.e., fit with CE01 templates rather than K15; blue squares) or AGN ($f(AGN)_{MIR} > 0.5$; red triangles) as a function of L_{IR} (left) and redshift (right). The small number statistics make it difficult to narrow down the true distribution of AGN with redshift, although it seems to be increasing.

3.2. Determining What Powers the Mid-IR Emission

K17 predicted that MIRI observations alone could be used to quantify AGN emission. We test that prediction by estimating the AGN fraction, $f(AGN)_{MIR}$, by initially fitting only the template library from K15 to the MIRI data. Template fitting is a complementary technique to full SED decomposition. The advantages of fitting templates are that it is less computationally expensive, there are fewer parameters resulting in fewer degeneracies, and it can be performed when only a few photometric observations are available.

We fit the suite of templates to all galaxies that have two or more MIRI photometric points with S/N > 3.0. We only include the MIRI data in this initial fitting, since this is the range that the templates are most sensitive to. We only fit one parameter, which is the scaling of the template to the photometry. To assess the goodness of fit, we calculate a reduced χ^2 parameter, and we accept all fits with reduced $\chi^2 = 0.5$–2.0. We then visually inspect the fits and overplot the Spitzer/IRAC, MIPS, and HST/WFC3 (F125W, F160W) photometry. 98% of galaxies with $L_{IR} \geqslant 10^{11} L_\odot$ and 70% of galaxies with $10^{10} L_\odot \leqslant L_{IR} < 10^{11} L_\odot$ are well fit with the K15 templates. This is not surprising, since the templates were created from IR-luminous galaxies with $L_{IR} \sim 10^{11}$–$10^{12} L_\odot$. Compellingly, upon visual inspection, the non-MIRI photometry follows the best-fitting template as well.

However, the low-luminosity galaxies probed by MIRI are very poorly described by the K15 template library below the mid-IR regime. Even when the reduced χ^2 is acceptable, visual inspection shows that the observed near-IR emission is brighter by an order of magnitude or more than the template emission.

In order to better capture the emission of lower-luminosity galaxies, we expanded the template fitting to include templates from the CE01 library. We fit the K15 and CE01 templates, this time including the Spitzer/IRAC 4.5 μm data point in the fitting to help anchor the ratio of near- to mid-IR emission. We integrate each best-fit template from 8 to 1000 μm to estimate the galaxy's infrared luminosity. As stated in Section 2.1, we are able to achieve good template fits for 482 galaxies, and

these galaxies comprise the final sample. Interestingly, we find that the best-fitting CE01 template L_{IR} does not necessarily correlate with the galaxy L_{IR} derived from the renormalized SED templates. In $\sim$40% of cases, these numbers differed by more than an order of magnitude.

In the initial fitting, where only the MIRI data points were fit with the K15 templates, a surprising 43% of galaxies with $L_{IR} < 10^{11} L_\odot$ were classified as AGN ($f(AGN)_{MIR} > 0.5$). When the 4.5 μm data point was included, along with the CE01 templates, this number dropped to 10%. Through our template fitting, we identify 28 AGN ($f(AGN)_{MIR} > 0.5$) out of our final sample of 482 galaxies. For context, Yang et al. (2023a) fit UV-MIRI photometry with CIGALE for our same sample, and they identify 31 AGN. We compare our template fitting results with the CIGALE decomposition and find good overall agreement. For 60% of the sources, the AGN fractions agree to within 10%, and for 95% of the sources, the fractions agree to within 50%. Broadly speaking, both manners of measuring $f(AGN)_{MIR}$ will classify the same galaxies as AGN, although the exact fractions may vary.

The K15 templates were created from dust-rich galaxies with strong PAH emission, and the ratio of mid- to near-IR emission reflects the fact that most of the galaxy's energy is being emitted in the infrared. In contrast, the lower-luminosity CE01 templates represent galaxies with less mid-IR emission compared with the strength of their near-IR emission. We label the sources best fit with the CE01 templates as "mid-IR weak" galaxies. Figure 3 shows how the AGN and mid-IR weak fractions vary with luminosity and redshift. As expected, the mid-IR weak fraction increases sharply below $L_{IR} = 10^{10} L_\odot$. The fraction of mid-IR weak galaxies decreases with redshift, although this is likely driven by the flux limit of the survey. The fraction of galaxies that are AGN increases with redshift. The increase in AGN is similar to what was found in Yang et al. (2023a). The increase in the number of detected AGN is likely due to their enhanced emission around 5 μm compared with star-forming galaxies, making them easier

Table 2
Properties of Luminosity Bins and SEDs

Bin (log L_{IR})	Sources	Median log L_{IR} [a] ($L_\odot$)	Median z	Average SED log L_{IR} [b] ($L_\odot$)
<9.0	50	8.52 [8.22, 8.77]	0.58 [0.41, 0.68]	8.44 [0.55]
9.0–9.5	54	9.26 [9.13, 9.38]	0.90 [0.74, 1.23]	9.02 [0.06]
9.5–10.0	79	9.74 [9.65, 9.86]	1.33 [0.92, 1.55]	9.53 [0.07]
10.0–10.5	77	10.24 [10.10, 10.38]	1.32 [0.79, 1.82]	9.88 [0.06]
10.5–11.0	43	10.72 [10.59, 10.90]	1.42 [1.08, 1.89]	10.29 [0.04]
11.0–11.5	39	11.14 [11.09, 11.31]	1.57 [1.19, 2.15]	10.66 [0.04]
>11.5	35	11.75 [11.55, 11.94]	1.53 [1.32, 1.81]	11.26 [0.04]

Notes.
[a] Median log L_{IR} and redshift (with lower and upper quartiles) for sources per bin. L_{IR} is extrapolated for individual sources using the best-fitting K15 or CE01 template.
[b] Average L_{IR} (with standard deviation) of log L_{IR} values extrapolated by fitting the average SED per luminosity bin using several different template libraries.

to detect in the longer-wavelength MIRI filters at higher redshift.

3.3. Average Emission of Mid-IR Selected Galaxies

MIRI has opened a deeper window on the infrared Universe, particularly at cosmic noon. We explore the ratio of near- to mid-IR emission in MIRI galaxies through the creation of average SEDs. We sort galaxies into luminosity bins of log $L_{IR} = 0.5$ dex, which allows for at least 35 galaxies in each bin. We then calculate the median L_{IR} in each bin and normalize each galaxy to that value. The L_{IR}s used to sort and normalize the galaxies are those derived by fitting the K15 and CE01 templates. We discuss L_{IR} further below. We remove all galaxies with $f(AGN)_{MIR} > 0.3$. We list the properties of each luminosity bin in Table 2.

We include the HST/ACS (F606W, F814W), WFC3 (F125W, F160W), Spitzer/IRAC, MIPS 24 μm, and MIRI photometry, redshifted to the rest frame, in the creation of the SEDs. We use a bootstrap technique, where we resample the sources in each bin with replacement 1000 times. In each iteration, we calculate the median luminosity in wavelength bins of differential sizes. After 1000 iterations, we calculate the average luminosity in each bin (this is the average of the median luminosities calculated in each iteration) and the standard deviation. We list these values in Table 3. Figure 4 shows all of the galaxies in each luminosity bin and the resulting average SED. It is notable that the noisiest photometry in each bin occurs around $\lambda \sim 5.0\,\mu$m, where the emission switches from being dominated by the older stellar population to being dominated by dust. The highest luminosity bin shows the most uniformity among individual galaxies.

Figure 5 shows the average SEDs in the left panel. The lower-luminosity SEDs clearly have more of their energy being radiated in the near-IR, which could indicate that the bulk of their star formation is unobscured. We explore this further in Section 4. We test whether the shape of the SED changes from $z = 0$ to cosmic noon by comparing with the CE01 templates in the right panel of Figure 5. We plot the CE01 template with L_{IR} closest to each average SED. Each CE01 template and average SED of a given luminosity has been arbitrarily normalized (the same normalization is applied to each set of a given luminosity) to allow for easier comparison. The average SEDs are in general remarkably similar to the CE01 SEDs, indicating that the relative amounts of near- and mid-IR emission do not

evolve strongly with redshift for galaxies of the same infrared luminosity. However, it is notable that the shape of the near-IR emission does change quite strongly for most of the luminosity bins. The MIRI templates lack the strong emission seen at 1.6 μm in the CE01 templates. This may reflect a difference in the ages of the stellar populations. The CE01 templates were created from local galaxies that have had an additional $\sim$6–9 billion yr to evolve, which can make the stellar population much older and the resulting emission much stronger in the near-IR.

As a caveat, L_{IR} for individual sources was calculated by simply integrating the best-fit K15 or CE01 template from 8 to 1000 μm, and the L_{IR} for each bin listed in Table 2 is the median of these values. Very few galaxies in these CEERS MIRI fields have direct far-IR detections from Herschel, so L_{IR} is an extrapolation from the mid-IR. If the ratio of mid- to far-IR emission is insensitive to redshift, then the L_{IR} of fainter galaxies (those missed by Herschel) can be accurately estimated from local templates.

We also calculate L_{IR} by fitting a suite of IR templates from CE01, Dale & Helou (2002), Draine & Li (2007), and Rieke et al. (2009) to each average SED (Table 3) at $\lambda_{rest} \geqslant 4.7\,\mu$m. Table 2 lists the average and standard deviation of the $\log(L_{IR})$ values extrapolated using these four template libraries. The average $\log(L_{IR})$ is about 0.5 dex smaller than the median $\log(L_{IR})$ values for individual sources per bin that were derived using the K15+CE01 templates. Except for the lowest luminosity bin, the standard deviations are small ($\leqslant$0.1 dex), showing that existing SED libraries have broadly consistent mid-to-total-IR luminosity ratios, i.e., that the choice among current-generation SED templates does not have a large impact on the total IR luminosities that we infer from MIRI data. The difference between the average and median $\log(L_{IR})$ values is especially noticeable in the higher luminosity bins. The reasons for this difference are twofold. (1) The stacked SEDs have artificially weaker PAH features than the template libraries. This is due to the stacked SEDs being derived from photometry, while the template libraries are based on models with much higher wavelength resolution. The apparently weaker PAH features can cause lower-luminosity models to be the best fit. (2) The K15 templates are empirically derived from higher-redshift galaxies, and the shape of the far-IR emission is slightly different from local templates (Kirkpatrick et al. 2012). In the higher luminosity bins, the majority of

Table 3
Average SEDs

Wavelength (μm)	L_ν (W Hz^{-1})	Unc. (W Hz^{-1})	L_ν (W Hz^{-1})	Unc. (W Hz^{-1})	L_ν (W Hz^{-1})	Unc. (W Hz^{-1})	L_ν (W/Hz)	Unc. (W/Hz)
	$\log L_{IR} < 9.0 L_\odot$		$\log L_{IR} = 9.0$–$9.5 L_\odot$		$\log L_{IR} = 9.5$–$10.0 L_\odot$		$\log L_{IR} = 10.0$–$10.5 L_\odot$	
0.335	3.66e20	7.97e19	1.24e21	1.57e20	2.14e21	2.98e20	2.30e21	2.55e20
0.454	6.90e20	1.08e20	2.36e21	2.36e20	5.96e21	7.42e20	6.10e21	6.39e20
0.544	7.91e20	1.21e20	2.49e21	5.00e20	6.25e21	8.16e20	8.19e21	9.12e20
0.663	8.32e20	1.38e20	2.98e21	3.06e20	6.24e21	5.70e20	8.06e21	7.60e20
0.913	1.14e21	1.32e20	3.74e21	2.89e20	7.78e21	1.06e21	9.91e21	1.39e21
1.330	1.20e21	1.41e20	4.33e21	3.17e20	1.02e22	7.18e20	1.44e22	3.56e21
1.740	9.60e20	9.93e19	3.69e21	2.16e20	9.17e21	7.31e20	1.25e22	2.16e21
2.243	8.94e20	4.25e19	2.92e21	2.38e20	7.14e21	9.80e20	1.01e22	1.18e21
2.750	6.63e20	5.02e19	1.86e21	1.88e20	6.21e21	7.93e20	7.99e21	9.35e20
3.220	6.64e20	5.81e19	1.93e21	1.82e20	4.58e21	4.17e20	6.92e21	1.15e21
3.722	6.62e20	6.59e19	1.42e21	4.00e20	4.67e21	8.32e20	6.48e21	1.45e21
4.462	4.67e20	5.32e19	1.43e21	9.95e19	3.73e21	6.27e20	4.65e21	5.52e20
5.284	3.78e20	4.36e19	1.48e21	1.29e20	4.18e21	6.19e20	7.21e21	1.33e21
5.797	4.51e20	6.12e19	1.63e21	2.54e20	5.06e21	5.44e20	1.06e22	1.07e21
6.310	4.71e20	5.90e19	2.20e21	2.94e20	6.89e21	1.01e21	1.67e22	1.85e21
6.784	6.38e20	7.38e19	3.87e21	4.07e20	7.08e21	1.33e21	2.05e22	2.08e21
7.269	6.91e20	7.97e19	4.17e21	3.66e20	1.31e22	1.22e21	3.00e22	4.30e21
7.635	8.03e20	1.18e20	5.03e21	4.15e20	1.33e22	2.15e21	3.32e22	1.69e21
8.259	8.75e20	1.02e20	4.93e21	4.02e20	1.24e22	1.08e21	2.98e22	1.80e21
8.683	7.23e20	1.21e20	3.42e21	6.18e20	1.33e22	1.88e21	2.68e22	2.66e21
9.731	7.53e20	1.07e20	3.71e21	2.88e20	8.78e21	6.21e20	2.11e22	2.85e21
10.919	1.00e21	1.83e20	4.37e21	5.27e20	1.33e22	1.50e21	2.79e22	6.23e21
12.052	1.12e21	1.35e20	4.75e21	5.47e20	1.39e22	2.67e21	3.22e22	3.94e21
13.908	9.27e20	1.91e20	2.86e21	2.02e20	8.21e21	7.60e20	3.80e22	5.43e21
16.462	9.50e20	1.68e20	2.76e21	1.85e20	1.12e22	1.66e21	3.57e22	2.83e21
	$\log L_{IR} = 10.5$–$11.0 L_\odot$		$\log L_{IR} = 11.0$–$11.5 L_\odot$		$\log L_{IR} > 11.5 L_\odot$			
0.335	3.97e21	4.47e20	7.31e21	2.75e21	5.21e21	2.06e21		
0.454	8.55e21	2.11e21	8.62e21	1.26e21	1.58e22	2.92e21		
0.544	1.24e22	3.34e21	1.38e22	3.02e21	1.94e22	3.28e21		
0.663	1.27e22	1.95e21	2.08e22	3.08e21	3.48e22	6.27e21		
0.913	2.00e22	9.34e21	2.87e22	6.26e21	6.61e22	1.41e22		
1.330	1.84e22	5.82e21	2.86e22	1.49e21	7.97e22	8.70e21		
1.740	1.84e22	1.60e21	3.24e22	1.63e21	9.16e22	8.06e21		
2.243	1.50e22	1.90e21	2.69e22	1.44e21	8.44e22	4.86e21		
2.750	1.79e22	5.37e21	2.27e22	1.59e21	6.52e22	9.99e21		
3.220	1.15e22	2.24e21	2.43e22	1.53e21	7.50e22	2.96e21		
3.722	1.00e22	1.01e21	2.28e22	1.29e21	8.07e22	5.04e21		
4.462	1.18e22	1.76e21	2.07e22	1.32e21	8.31e22	6.66e21		
5.284	1.37e22	2.26e21	3.09e22	4.60e21	1.32e23	1.62e22		
5.797	2.49e22	4.67e21	5.70e22	7.32e21	2.53e23	4.62e22		
6.310	4.07e22	3.79e21	1.00e23	1.34e22	4.67e23	2.32e22		
6.784	5.54e22	7.34e21	1.44e23	2.00e22	5.30e23	4.59e22		
7.269	8.39e22	9.27e21	2.10e23	2.48e22	7.79e23	1.06e23		
7.635	1.08e23	2.35e22	2.52e23	4.26e22	1.09e24	7.23e22		
8.259	9.49e22	4.55e21	2.58e23	3.15e22	9.74e23	7.57e22		
8.683	9.37e22	1.48e22	2.27e23	4.10e22	8.25e23	2.20e23		
9.731	5.00e22	1.64e22	1.50e23	5.35e22	5.93e23	1.63e23		
10.919	8.87e22	2.47e22	1.44e23	2.50e22	5.37e23	1.08e23		
12.052	7.64e22	1.17e22	2.25e23	7.95e22	9.58e23	2.87e22		
13.908	7.83e22	1.29e22	1.92e23	2.91e22	6.40e23	9.71e22		
16.462	6.51e22	0.00e00	1.61e23	9.23e21	6.45e23	4.16e22		

sources were fit with the K15 library, which can also contribute to the difference in L_{IR} when compared with the results from locally derived libraries.

Although the various template libraries largely agree with one another when used to extrapolate L_{IR} from the mid-IR emission, it is important to bear in mind that these libraries have been calibrated on local sources or infrared-luminous galaxies. The ratio of mid- to far-IR emission can change with location on the main sequence, redshift, and metallicity (Elbaz et al. 2011; Kirkpatrick et al. 2017b; Schreiber et al. 2018).

Direct far-IR measurements for the low-luminosity, high-redshift MIRI galaxies would be necessary to verify their total
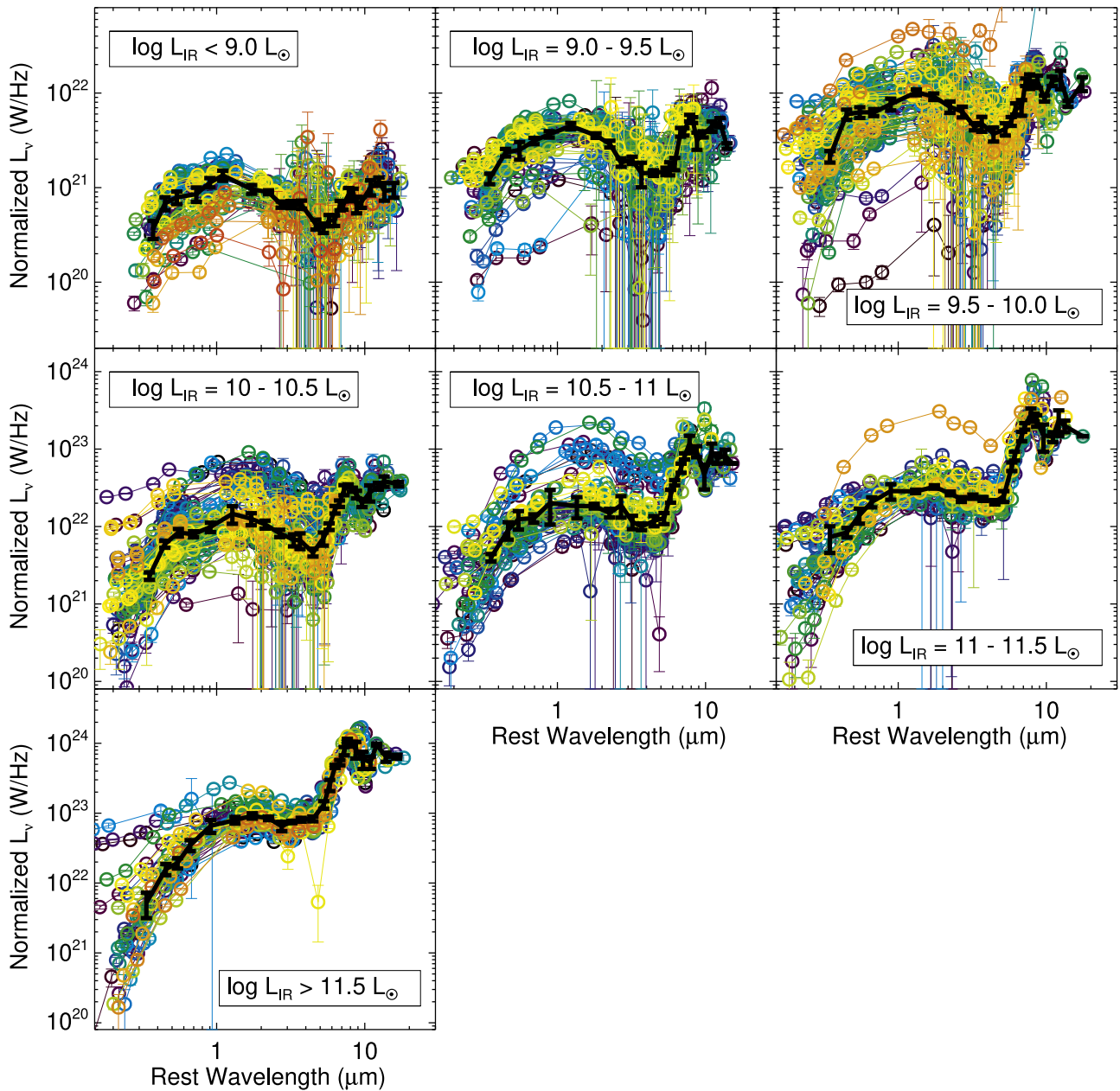
Figure 4. To create average SEDs (shown in black), we separated galaxies by luminosity and normalized to the median luminosity in each bin. Individual galaxies are plotted by color.

luminosities. While deep millimeter observations with ALMA, LMT/TolTEC, or other facilities can provide some constraint at wavelengths beyond the peak of bolometric emission, ultimately, a new, sensitive far-IR observatory will be required to robustly measure L_{IR} for these galaxies.

3.4. Color Selection

K17 used the K15 templates to predict where AGN would lie when combining MIRI photometric bands for color selection. MIRI color selection of AGN is hampered by two facts. First, with just a few closely spaced photometric points, star-forming galaxies can mimic a power law in the mid-IR. Therefore, MIRI color selection of AGN only has a unique solution when the redshift is known. Second, if only mid-IR photometry is used, mid-IR weak galaxies can mimic the weak PAH features

in AGN. We find that when plotting the real CEERS observations in the MIRI color spaces presented in K17, the AGN regions are severely contaminated by the mid-IR weak galaxies.

Instead, we present a new diagnostic that does not take into account redshift information in order to illustrate the limited utility of using mid-IR colors alone to identify AGN. Figure 6 combines the colors S_{F1800W}/S_{F1000W} with S_{F1280W}/S_{F1000W}. We find that combining three filters, rather than four, does a better job at separating AGN, star-forming galaxies, and mid-IR weak galaxies.

The dust-rich galaxies (those fitted with K15 templates) are plotted as colored circles, while the mid-IR weak galaxies (fit with CE01 templates) are plotted as gray squares. AGN (solid circles) lie toward the center of the color space, while star-forming galaxies lie around the edges.
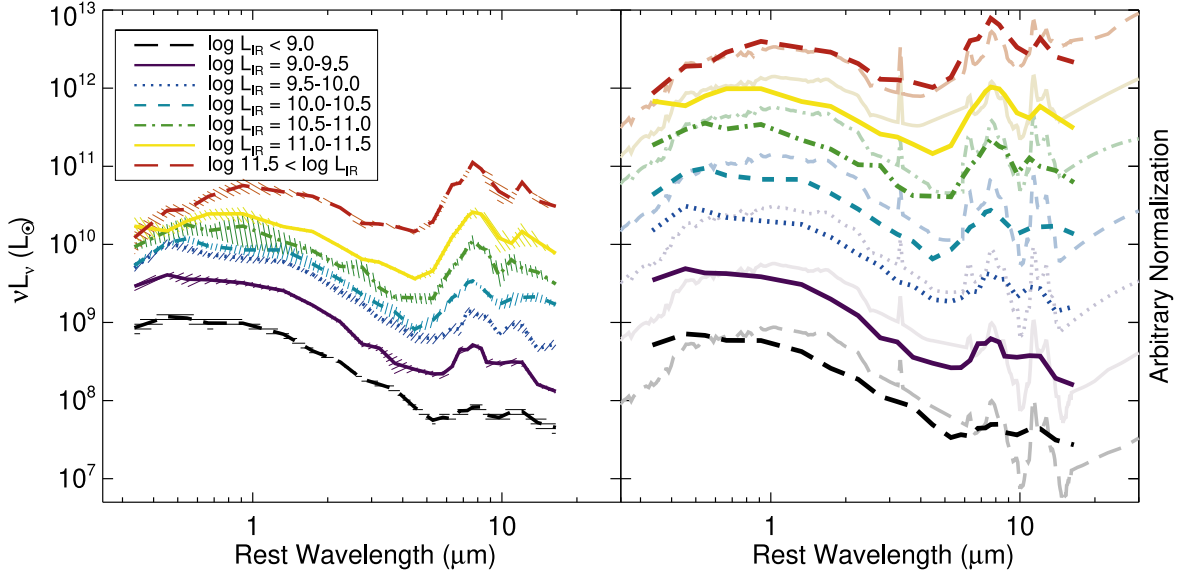
Figure 5. Left panel: average SEDs from Figure 4. The PAH features clearly become stronger with increasing luminosity. At low luminosities, the mid-IR emission is much weaker than the near-IR emission. Right panel: average SEDs are plotted alongside the CE01 template of the same L_{IR}. Arbitrary normalization is applied to templates of the same luminosities. The CE01 templates have more emission around $\lambda \sim 1.6 \ \mu m$, which may be attributable to their older stellar populations.

We define an irregular hexagon to separate the AGN from the non-AGN, the vertices of which are

$$x = \log(S_{F1800W}/S_{F1000W})$$
$$y = \log(S_{F1280W}/S_{F1000W})$$
$$[x, y] = [0.04, 0.15], [0.04, 0.44],$$
$$[0.24, 0.79], [0.47, 0.79],$$
$$[0.25, 0.44], [0.25, 0.15]. \quad (1)$$

Within this region, there are 19 AGN and 48 contaminants (there are 25 AGN total in this figure). Without including redshift information, this reliability (28%) is the best that can be achieved with MIRI colors alone.

Galaxies with PAH features move in the diagram as redshift increases. The star-forming galaxies move from the bottom of the plot at $z < 0.6$ to the top right at $z \sim 0.6$–1.5 (the redshift track is illustrated with the purple dashed line). At greater redshifts, they move toward the middle left. The mid-IR weak galaxies (redshift tracks are the magenta and pink dotted–dashed lines) follow the same general movement but at lower color ratios, causing them to contaminate the region predominantly occupied by AGN. The AGN, due to their lack of PAH features, do not greatly change location due to redshift.

As seen in the left panel of Figure 6, mid-IR weak galaxies contaminate the AGN region mostly at $z \sim 1$. The reason for this is illustrated in the right panel. We have plotted the K15 MIR1.0 template and our $\log L_{IR} = 9.0$–9.5 and 10.0–10.5 SEDs from this work. We overplot the MIRI F1000W, F1280W, and F1800W filters, shifted to the rest wavelength they would have at $z = 1$. At this redshift, there simply is not a wide separation between the SEDs, so intrinsic variation between sources will cause overlap between AGN and mid-IR weak colors. It is also obvious that adding a power-law criterion (i.e., F1000W < F1280W < F1800W) will not help the situation, as that can be true for galaxies with and without PAH features in this regime. The part of the SEDs with the largest separation is the near-IR.

Figure 7 shows the filters where the three templates (plotted on the figure) have the strongest separation over the

largest range of redshifts. The inclusion of a near-IR data point can help separate mid-IR weak galaxies from dust-rich galaxies. We combine IRAC and MIRI data to measure $\log S_{F1800W}/S_{3.6 \ \mu m}$ and $\log S_{F1000W}/S_{3.6}$. We use IRAC rather than NIRCam due to the uneven coverage of the CEERS observations.

The mid-IR weak galaxies (gray squares) lie in the lower left region of this color space, while the dust-rich galaxies lie in the upper left. The threshold $S_{F1000W}/S_{3.6} \geqslant 0.35$ separates dust-rich star-forming galaxies from mid-IR weak galaxies. Given the difference in luminosities between these classes of galaxies, it can also be seen as an infrared luminosity threshold. Dust-rich star-forming galaxies at $z < 1$ are the main contaminant in the upper right, where the AGN predominately lie. We recommend the following criteria for selecting AGN:

$$x = \log(S_{F1800W}/S_{3.6})$$
$$y = \log(S_{F1000W}/S_{3.6})$$
$$y \geqslant 0.55$$
$$y \geqslant 2.78x - 0.98$$
$$y \leqslant 1.92x + 0.45. \quad (2)$$

Within this region, there are 15 AGN and 13 contaminants. There are 22 total AGN shown in Figure 7.

The MIRI-only selection (Figure 6) has a reliability of 28%, while the MIR+NIR selection (Figure 7) has a reliability of 54%. If we combine the mid-IR criteria (Equation (1)) with the following criteria:

$$x = \log(S_{F1800W}/S_{3.6})$$
$$y = \log(S_{F1000W}/S_{3.6})$$
$$x \geqslant 0.55$$
$$y \geqslant 0.05, \quad (3)$$

then 13 AGN are selected (out of 22) with a mere five contaminants, giving a reliability of 72%. For AGN candidate selection in large surveys, we recommend combining Equations (1) and (3). However, for small surveys, where computational resources are not a concern, we recommend
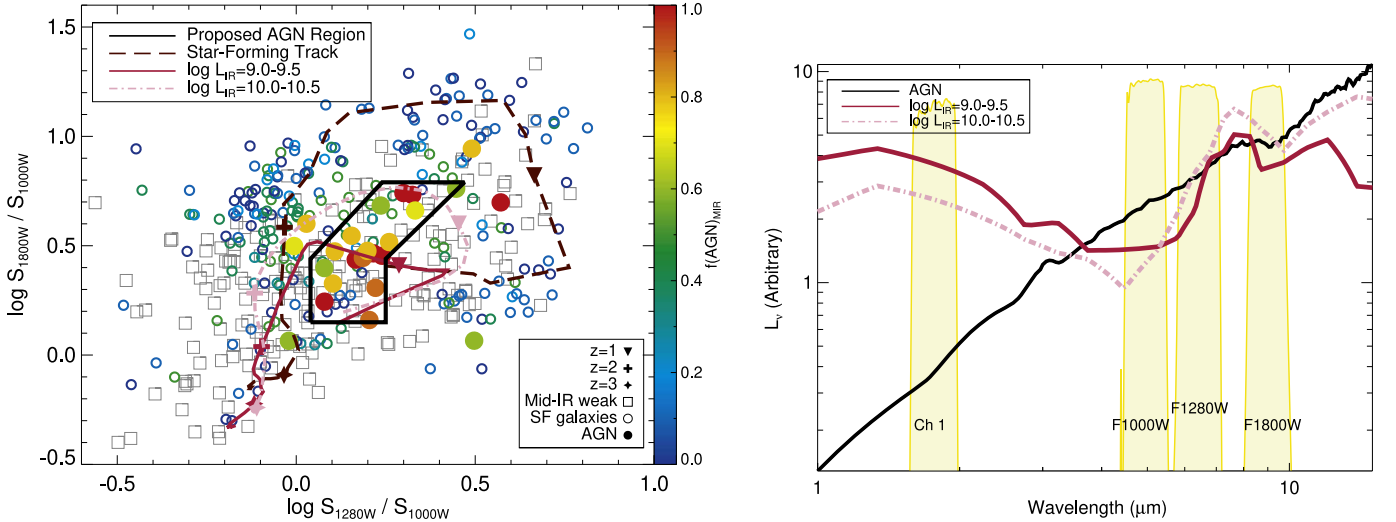
Figure 6. Left panel: MIRI color selection of AGN. Dust-rich galaxies (circles) are colored according to $f(AGN)_{MIR}$. Galaxies with $f(AGN)_{MIR} > 0.5$ are shown as filled circles. The mid-IR weak galaxies are the gray squares. The proposed AGN selection region (Equation (1)) is shown as the solid line. We illustrate how the dust-rich star-forming galaxies (purple dashed line; K15 template) and mid-IR weak galaxies (magenta and pink dotted–dashed lines; this work) move with redshift. AGN do not strongly evolve with redshift. Dust-rich galaxies separate by $f(AGN)_{MIR}$, while the mid-IR weak galaxies contaminate the AGN regions. Right panel: mid-IR weak SEDs compared with a K15 AGN template. The IRAC Ch 1 (3.6 μm) bandpass is shown alongside the MIRI bandpasses. All bandpasses have been redshifted to $z = 1$. At this redshift, the mid-IR weak and AGN templates have similar mid-IR colors, but the inclusion of a near-IR data point will help to separate them.
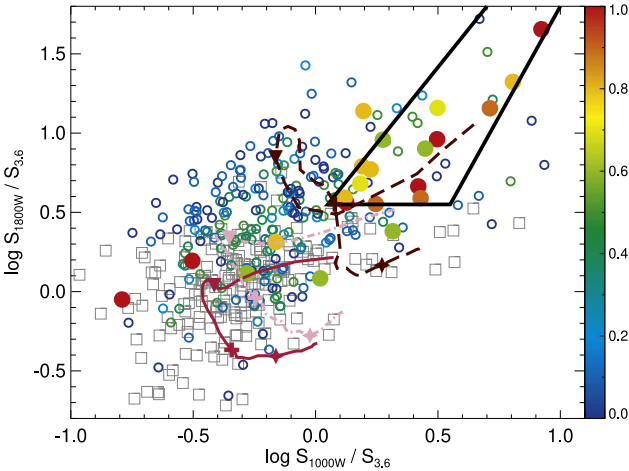

Figure 7. MIRI + near-IR color selection of AGN. Symbols and lines are the same as in Figure 6. Dust-rich galaxies separate from mid-IR weak galaxies, in contrast with Figure 6. The solid lines show our proposed AGN selection region. The main contaminant in this region is the dust-rich star-forming galaxies at $z < 1$.

template fitting or SED decomposition, as color selection lacks either completeness or reliability.

3.5. Number Counts

We present cumulative number counts of the 10 μm sources in Figure 8 and Table 4. Overall, there were 573 galaxies with a $>3\sigma$ detection at 10 μm (observed frame) and 469 10 μm–detected galaxies in the final sample that have been fit with templates (these numbers differ slightly from Section 2.1 because here we are describing sources with a 10 μm detection, rather than a detection at any wavelength). At the peak redshift distribution of the MIRI sources, $z = 1.4$, the F1000W bandpass is probing rest-frame 4 μm emission.

We compare the 10 μm counts with the IRAC 8 μm counts from Fazio et al. (2004) in the EGS and Boötes fields. The EGS
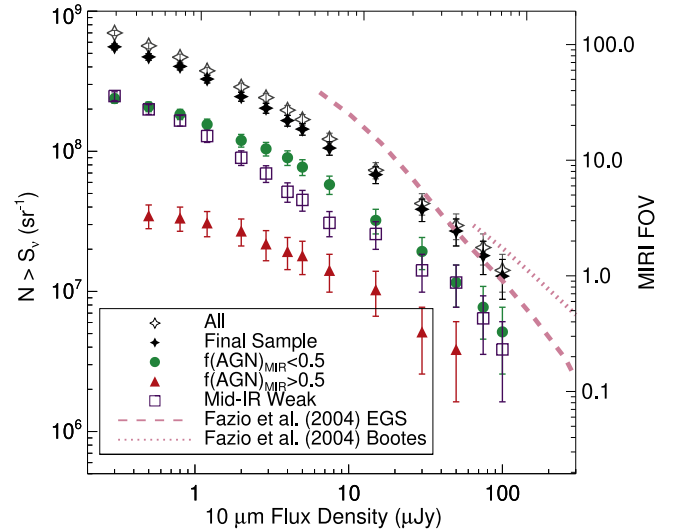

Figure 8. 10 μm cumulative number counts for all sources with S/N > 3 in F1000W (open stars) and the final sample (filled stars). Our selection criteria mainly affected sources at the faintest F1000W fluxes. We also show the number counts for the mid-IR weak galaxies (blue squares), star-forming galaxies ($f(AGN)_{MIR} \leqslant 0.5$; filled green circles), and AGN ($f(AGN)_{MIR} > 0.5$; red triangles). AGN predominantly have brighter F1000W fluxes. The 8 μm number counts from Fazio et al. (2004) are shown in pink. The discrepancy between the 8 and 10 μm counts may be due to the large differences in field sizes. The number of sources in one MIRI FOV is shown on the right axis.

counts match the 10 μm counts at the bright end, although the Boötes counts are higher. In the midrange (10 μJy), the MIRI and IRAC counts also disagree. This could possibly be attributed to the much small area in the MIRI survey compared with the IRAC data. A mere 67 sources have $S_{F1000W} = 8.0$–80.0 μJy, which could make the underlying distribution of the parent population difficult to distinguish. A large-area MIRI survey will better determine the true flux distribution of galaxies.

Table 4
10 μm Cumulative Number Counts

$S_{1000W}(\mu Jy)$	All Sources	Final Sample	$f(AGN)_{MIR} \leqslant 0.5$	$f(AGN)_{MIR} > 0.5$	Mid-IR Weak Sources
0.3	$6.99 \pm 0.30 \times 10^8$	$5.58 \pm 0.27 \times 10^8$	$2.39 \pm 0.18 \times 10^8$	$\cdots$	$2.45 \pm 0.18 \times 10^8$
0.5	$5.65 \pm 0.27 \times 10^8$	$4.73 \pm 0.25 \times 10^8$	$2.08 \pm 0.16 \times 10^8$	$3.47 \pm 0.67 \times 10^7$	$1.98 \pm 0.16 \times 10^8$
0.8	$4.69 \pm 0.25 \times 10^8$	$4.05 \pm 0.23 \times 10^8$	$1.85 \pm 0.15 \times 10^8$	$3.34 \pm 0.66 \times 10^7$	$1.63 \pm 0.15 \times 10^8$
1.2	$3.75 \pm 0.22 \times 10^8$	$3.29 \pm 0.21 \times 10^8$	$1.54 \pm 0.14 \times 10^8$	$2.96 \pm 0.62 \times 10^7$	$1.30 \pm 0.13 \times 10^8$
2.0	$2.88 \pm 0.19 \times 10^8$	$2.45 \pm 0.18 \times 10^8$	$1.18 \pm 0.12 \times 10^8$	$2.57 \pm 0.58 \times 10^7$	$9.00 \pm 1.08 \times 10^7$
2.9	$2.42 \pm 0.18 \times 10^8$	$2.03 \pm 0.16 \times 10^8$	$1.05 \pm 0.12 \times 10^8$	$2.18 \pm 0.53 \times 10^7$	$6.68 \pm 0.93 \times 10^7$
4.0	$1.97 \pm 0.16 \times 10^8$	$1.66 \pm 0.15 \times 10^8$	$9.12 \pm 1.08 \times 10^7$	$1.93 \pm 0.50 \times 10^7$	$4.88 \pm 0.79 \times 10^7$
5.0	$1.68 \pm 0.15 \times 10^8$	$1.44 \pm 0.14 \times 10^8$	$7.84 \pm 1.00 \times 10^7$	$1.80 \pm 0.48 \times 10^7$	$4.37 \pm 0.75 \times 10^7$
7.5	$1.22 \pm 0.13 \times 10^8$	$1.05 \pm 0.11 \times 10^8$	$5.78 \pm 0.86 \times 10^7$	$1.41 \pm 0.43 \times 10^7$	$3.08 \pm 0.63 \times 10^7$
15.0	$7.33 \pm 0.97 \times 10^7$	$6.81 \pm 0.94 \times 10^7$	$3.21 \pm 0.64 \times 10^7$	$1.03 \pm 0.36 \times 10^7$	$2.57 \pm 0.58 \times 10^7$
30.0	$4.24 \pm 0.74 \times 10^7$	$3.86 \pm 0.70 \times 10^7$	$1.93 \pm 0.50 \times 10^7$	$5.14 \pm 2.57 \times 10^6$	$1.41 \pm 0.43 \times 10^7$
50.0	$2.96 \pm 0.62 \times 10^7$	$2.70 \pm 0.59 \times 10^7$	$1.16 \pm 0.39 \times 10^7$	$3.86 \pm 2.23 \times 10^6$	$1.16 \pm 0.39 \times 10^7$
75.0	$2.06 \pm 0.51 \times 10^7$	$1.80 \pm 0.48 \times 10^7$	$7.71 \pm 3.15 \times 10^6$	$\cdots$	$6.43 \pm 2.87 \times 10^6$
100.0	$1.41 \pm 0.43 \times 10^7$	$1.29 \pm 0.41 \times 10^7$	$5.14 \pm 2.57 \times 10^6$	$\cdots$	$3.86 \pm 2.23 \times 10^6$

We also show the number counts of the mid-IR weak, star-forming ($f(AGN)_{MIR} \leqslant 0.5$), and AGN ($f(AGN)_{MIR} > 0.5$) populations. The faint galaxy population at cosmic noon contains a large fraction of mid-IR weak galaxies (Figure 3). Interestingly, both the mid-IR weak and dust-rich galaxies have approximately the same flux distribution. The mid-IR weak galaxies do not dominate the counts at faint fluxes. We find fewer than five AGN per MIRI pointing, illustrating that a large MIRI survey will be required to build up sufficient population statistics of infrared AGN. MIRI is capable of finding AGN in lower-luminosity galaxies and galaxies at higher redshift (Figure 3), but large areas are required due to the relative rarity of AGN.

4. Discussion

4.1. Where Are All the AGN?

K17 predicted finding a significant population of faint AGN at cosmic noon by extrapolating down the luminosity function based on the number of AGN observed in IR-luminous galaxies. The MIRI observations have revealed significantly fewer AGN at cosmic noon and high redshift than predicted in K17. This can be attributed to two reasons: AGN may be harder to identify than expected, or AGN may by intrinsically low luminosity in lower-mass galaxies. Distinguishing between the scenarios will require larger MIRI surveys in conjunction with spectroscopic or X-ray surveys.

The most luminous, unobscured AGN exhibit power-law emission in the near-IR, as well as the mid-IR. Heavily obscured AGN, however, may not be visible in the near-IR (Hickox & Alexander 2018, and references therein). The emission from the hottest regions of the torus will be reabsorbed by subsequent dust layers and reemitted at longer wavelengths. This reprocessing weakens the emission at shorter infrared wavelengths. The obscured fraction of AGN rises with increasing redshift (Yang et al. 2023a; Peca et al. 2023), which means that relying on rest-frame $\lambda < 5\,\mu$m photometric emission will likely miss a significant fraction of AGN beyond $z > 3$, when the MIRI filters no longer cover the mid-IR. Heavily obscured AGN may have a visible stellar bump arising from the host galaxy, although power-law emission should still be visible in the mid-IR (Lyu & Rieke 2022). In Figure 7, there are AGN that lie in the mid-IR weak region, outside of the proposed AGN selection area, indicating the diversity of near-IR emission exhibited by AGN. AGN with

$\log(S_{1800W}/S_{3.6}) < 0.5$ may be more obscured. Alternately, these could belong to a class of "hot dust-poor" type 1 AGN, which exhibit relatively weak near-IR emission (Hao et al. 2010; Lyu et al. 2017). The cause of the weak torus in these sources is unknown, but they have been observed out to $z = 6$.

Many galaxies show a mix of power-law AGN and PAH emission in the mid-IR. In practice, this manifests as weaker PAH features (Pope et al. 2008; Kirkpatrick et al. 2012; Sajina et al. 2012). Low-luminosity AGN that are accreting at high Eddington ratios will have power-law emission from a torus (Mason et al. 2012), but this emission may be outshone by the galaxy's star-forming component. In low-luminosity galaxies, weak PAH features may be due to swamping by an AGN, or they may be intrinsically weak due to the galaxy's dust content, as seen in Figure 5. Therefore, at low luminosity, weak PAH features are not a reliable means of identifying AGN. Additionally, low-luminosity AGN that accrete at low Eddington ratios may lack a torus altogether (Yuan & Narayan 2014). Intrinsically low-luminosity AGN ($L_X < 10^{42}$ erg s^{-1}) may be difficult or even impossible to identify with photometric information alone.

In both cases (high obscuration or low luminosity), there are promising ways forward. Hatcher et al. (2021) used mid-IR colors to identify AGN candidates that were not X-ray detected in the COSMOS field. The authors performed X-ray stacking to obtain the average emission of the AGN candidates and found that, indeed, as a population, the AGN candidates had X-ray signatures indicative of hosting a low-luminosity AGN. X-ray stacking remains a promising way to measure the average AGN emission of a population. Specific to JWST, nebular line diagnostics will also be useful (Backhaus et al. 2022), potentially more so than looking for broad-line emission, as low-luminosity AGN may lack a broad-line region (Elitzur et al. 2014). AGN emit multiple high-ionization nebular lines, including [Ne V], [Ne VII], and [O IV] (Cleri et al. 2023b, 2023a; Negus et al. 2023). Mid-IR spectroscopy may be the most reliable method for identifying obscured or low-luminosity AGN (Petric et al. 2011; Bonato et al. 2017; Stone et al. 2022).

With photometry alone, headway could possibly be made by spatially decomposing the galaxies into an inner and outer region. For the most massive galaxies, this may be possible, but, as is clear from Figure 1, most MIRI galaxies are small in size. This is likely due to the fact that MIRI is probing lower-mass galaxies. Finally, photometric or spectroscopic

identification of AGN may be made more reliable through machine-learning algorithms (Holwerda et al. 2021; Tardugno Poleo et al. 2023). Machine learning is capable of combining more photometric and color information than is possible with simple color selection. Machine learning can also take into account redshift information, which is useful in identifying the PAH features.

While identification challenges are a likely culprit for not finding more AGN at cosmic noon in our MIRI sample, there is also the possibility that bolometrically luminous AGN do not exist in large quantities in lower-luminosity ($L_{IR} < 10^{11} L_\odot$) galaxies. In isolated, low-luminosity galaxies, there may not be a large enough gas supply being funneled to the center of the galaxy to fuel black hole growth at high enough Eddington rates to be energetically dominant over the star formation and therefore detectable. Alternately, but similarly problematic, is the role that the AGN duty cycle may play. AGN in low-luminosity galaxies may accrete at large enough Eddington ratios to be detectable, but they may only do so for a short amount of time. If we make the simplifying assumption that all galaxies host detectable AGN at some point in their life, then the left panel of Figure 3 indicates that the duty cycle of these AGN is <10% of the star-forming time. In this scenario, we will never observe large numbers of AGN in low-luminosity galaxies because they are in their "dormant" phase.

4.2. PAH Emission

PAH emission arises at the edges of star-forming regions, and globally, the integrated PAH emission of a galaxy has been shown to correlate with its SFR. The link between PAH emission and star formation naturally leads to a correlation with L_{IR}, as L_{IR} is largely attributed to dust heating by stars formed within the past 100 Myr. PAH emission is frequently parameterized by the luminosity of the 6.2 μm feature, $L_{6.2}$. The ratio $L_{6.2}/L_{IR}$ is observed to decrease with increasing L_{IR}. Locally, this decrease is most evident in ULIRGs ($L_{IR} \gtrsim 10^{12} L_\odot$). The origin of decreasing PAH emission is debated, but one possibility is that the geometry of star-forming regions is changing. In ULIRGs, star formation predominantly occurs in a large, obscured nuclear starburst. This increases the volume of dust (increasing L_{IR}) while decreasing the surface area (decreasing $L_{6.2}$). In contrast, local LIRGs ($L_{IR} = 10^{11}$–$10^{12} L_\odot$) are more similar to normal star-forming galaxies in that they have many star-forming regions spread throughout the galaxy.

Intriguingly, the ratio of $L_{6.2}/L_{IR}$ is higher in ULIRGs at cosmic noon compared with local ULIRGs, indicating changing conditions of star formation (Pope et al. 2013; Kirkpatrick et al. 2014; McKinney et al. 2020). Studies of $L_{6.2}/L_{IR}$ in galaxies beyond the local Universe are rare, as previously, Spitzer/IRS was the only instrument capable of measuring $L_{6.2}$, and only in the brightest galaxies.

We take a first look at estimating $L_{6.2}/L_{IR}$ in galaxies at $z > 0$ using JWST down to an L_{IR} an order of magnitude lower than what was possible with Spitzer. The MIRI filters cover the 6.2 μm feature in different redshift ranges. We identify the redshift ranges for each filter where the 6.2 μm feature is isolated, and the rising continuum beyond 6.3 μm does not dominate the emission. We find the following redshift ranges suitable:
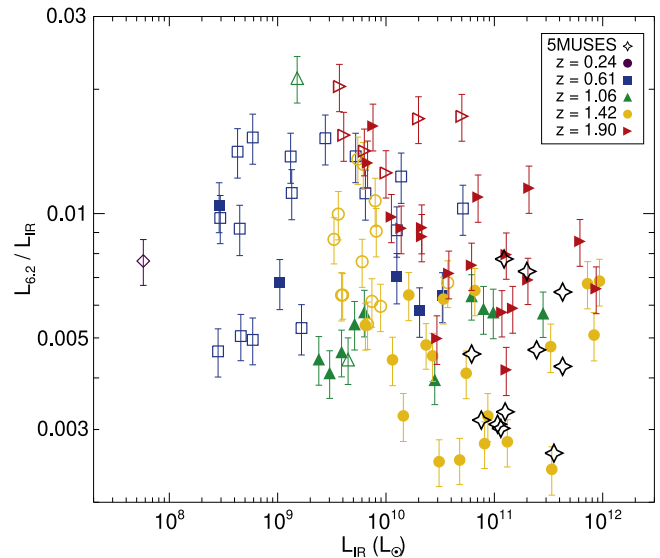
$$\text{F770W: } 0.20 < z < 0.28, \tag{4}$$

Figure 9. $L_{6.2}/L_{IR}$ vs. L_{IR} for the MIRI galaxies falling in the redshift ranges in Equation (8). $L_{6.2}$ has been estimated by calculating what percentage of the photometric point could be due to the 6.2 μm feature using the 5MUSES sample of star-forming galaxies from Kirkpatrick et al. (2014; black stars). The mid-IR weak galaxies are shown as the open symbols, while the filled symbols correspond to the dust-rich galaxies. Lower-luminosity galaxies have higher ratios of $L_{6.2}/L_{IR}$, in line with local trends. Interestingly, the higher-redshift sources seems to have higher $L_{6.2}/L_{IR}$, which could indicate a shift in the star-forming conditions at higher redshift. Spectroscopy is required to accurately measure $L_{6.2}$ and confirm this trend.

$$\text{F1000W: } 0.58 < z < 0.67, \tag{5}$$

$$\text{F1280W: } 1.04 < z < 1.11, \tag{6}$$

$$\text{F1500W: } 1.39 < z < 1.47, \tag{7}$$

$$\text{F1800W: } 1.87 < z < 1.95. \tag{8}$$

We do not include F2100W, as we do not have any sources in a suitable redshift range.

For each photometric point, we first estimate how much of the broadband photometry is potentially due to the 6.2 μm emission feature using a local sample with mid-IR spectroscopy. The 5MUSES sample was observed with Spitzer/IRS and has published $L_{6.2}$ and L_{IR} measurements in Kirkpatrick et al. (2014). That work contains 11 star-forming galaxies spanning $z = 0.06$–0.24, $\log L_{IR} = 10.79$–11.63 $L_\odot$, and a range of $L_{6.2}/L_{IR}$. The average (standard deviation) of $L_{6.2}/L_{IR}$ is 0.00456 (0.00181) for the 11 5MUSES galaxies.

We shift the 11 5MUSES Spitzer/IRS spectra to the redshift of each MIRI galaxy and convolve with the appropriate MIRI transmission filter to calculate νL_ν, or the photometric luminosity in a given MIRI bandpass. We use the published $L_{6.2}$ value and calculate $L_{6.2}/\nu L_\nu$ for all 11 5MUSES galaxies. We take the mean and standard deviation of $L_{6.2}/\nu L_\nu$ for the 11 galaxies as a scaling factor and associated uncertainty. We then multiply the MIRI photometry of each galaxy in our sample by this scaling factor to estimate $L_{6.2} [L_\odot]$ and an uncertainty. Figure 9 shows $L_{6.2}/L_{IR}$ as a function of L_{IR} for the MIRI sources. This is a conservative approach that marginalizes over uncertainty in the underlying SED based on what we expect from $z < 0.2$ galaxies. A caveat to this approach is that L_{IR} has been determined by fitting templates to all of the MIRI and IRAC photometry, which will include the data point used to calculate $L_{6.2}$. While these calculations are somewhat independent, spectroscopy is needed to fully uncouple them.

Figure 9 shows the same trend that is observed locally: $L_{6.2}/L_{IR}$ decreases with increasing L_{IR} for a fixed redshift bin. This decrease starts to happen noticeably around $L_{IR} = 10^{10} L_\odot$. This is the same luminosity where the near- and mid-IR photometry begins to be best fit by dusty star-forming templates from K15, rather than mid-IR weak templates from CE01. The conditions of star formation may be significantly different in these infrared-luminous sources. We show the mid-IR weak sources as open symbols, and they have higher $L_{6.2}/L_{IR}$ ratios. The decrease in $L_{6.2}/L_{IR}$ with increasing L_{IR} is then driven by a shift from predominantly mid-IR weak sources to dust-rich sources.

Figure 9 also hints at an increase in $L_{6.2}/L_{IR}$ at higher redshifts (red triangles compared with yellow circles), similar to what has been measured in sources with Spitzer/IRS spectroscopy (Pope et al. 2013). This shift could indicate that the geometry and physics of star formation are changing with increasing look-back time. For example, higher $L_{6.2}/L_{IR}$ ratios at earlier times could be a by-product of the higher gas fractions in high-redshift galaxies. Indeed, Cortzen et al. (2019) demonstrate that PAHs are good tracers of the cold molecular gas from $z \sim 0$ to 2, and galaxies at high redshift are increasingly gas-dominated, which would increase $L_{6.2}$ relative to the dust-obscured SFR measured by L_{IR}. Alternatively, McKinney et al. (2020) show that the offset in $L_{6.2}/L_{IR}$ for fixed L_{IR} between $z \sim 0$ and 2 galaxies disappears when normalizing L_{IR} by the IR size. This indicates that the geometry of distributed star formation across these galaxies also plays an important role in setting the $L_{6.2}/L_{IR}$ ratio. Of course, the reader should bear in mind two caveats: $L_{6.2}$ has been estimated from photometry, and L_{IR} has been extrapolated from near- and mid-IR photometry. Robustly testing how the PAH fraction changes with luminosity and redshift will require JWST spectroscopic observations and a new far-IR telescope.

4.3. The Nature of Mid-IR Weak Sources

We designated sources as mid-IR weak or dust-rich based on which set of templates fit them best. Mid-IR weak sources have a much larger near-IR/mid-IR emission ratio. The mid-IR weak status has a few potential explanations. First, these galaxies may be dust-poor, so the mid-IR emission overall is weaker than the near-IR emission, but the dust grain size distribution (i.e., PAH fraction) is similar to the dust-rich galaxies. On the other hand, these galaxies may be metal-poor, so that the PAH features are weaker. Finally, weaker mid-IR emission may be caused by a change in dust-heating mechanisms. In the local Universe, spatially resolved modeling of the mid- and far-IR emission shows that the temperature of dust in lower-mass galaxies is lower due to the dusty disk being more extended than the stellar disk (Trewhella et al. 2000; Dalcanton et al. 2004; Xilouris et al. 2004; Holwerda et al. 2009, 2012). The weak mid-IR emission is then attributable to most of the dust in low-mass galaxies being colder. Morphological studies with MIRI and NIRcam may be able probe the extent of the dust and stars in $z \sim 1$–2 galaxies (Magnelli et al. 2023; Shen et al. 2023).

The high $L_{6.2}/L_{IR}$ ratios in the mid-IR weak galaxies (Figure 9) hint that decreasing PAH emission (and hence low metallicity) is not to blame for the changing near-IR/mid-IR ratios. We also test this by fitting the average SEDs (Table 3) with the Draine & Li (2007) dust models, in which the spectra are fit with models heated by radiation fields of different strengths for mixtures of amorphous silicate and graphite grains, including varying amounts of PAH particles. We find that all but two of the SEDs have the exact same $q_{PAH} = 4.58$ as measured by these models. The $\log L_{IR} < 9.0$ and $\log L_{IR} = 10.0$–10.5 SEDs have $q_{PAH} = 2.50$. These results imply that the PAH spectrum is quite homogeneous for all of our galaxies, although the PAH emission only rises above the 1.6 μm stellar bump for galaxies at higher L_{IR}. This is in fact different from how models such as CE01 or Rieke et al. (2009) behave, as the PAH features in those models become more obscured by a dust continuum at higher L_{IR} values. In contrast, the K15 templates have much stronger PAH features than local templates of the same luminosities.

If we take Figure 9 at face value, the interpretation of the mid-IR weak sources becomes that their overall dust emission is weak, but they are not metal-poor. The similar q_{PAH} values point to similar amounts of very small grains regardless of luminosity. The higher $L_{6.2}/L_{IR}$ in mid-IR weak galaxies points to a lack of far-IR emission, which would rule out the interpretation that their dust is colder. Future far-IR observations would provide interesting insights into the interstellar mediums of this relatively unexplored population.

4.4. How Do MIRI SFRs Correlate with Optical SFRs?

In dust-rich galaxies, infrared SFRs are more reliable than optical SFRs, since much of the optical emission is attenuated (Kennicutt 1998; Calzetti et al. 2007; Kennicutt & Evans 2012; Boquien et al. 2016). It is therefore tempting to use IR observations to calculate SFRs for all infrared-detected galaxies. However, MIRI observations probe further down the luminosity function at cosmic noon than previous IR telescopes, and most CEERS MIRI sources are undetected by the available Herschel observations. This can introduce significant uncertainty into the calculation of L_{IR}, as the ratio of far- to mid-IR emission has intrinsic scatter and can also depend on factors such as metallicity and whether galaxies are on the main sequence (Elbaz et al. 2011). In this section, we compare previously calculated optical SFRs with SFRs estimated by our simplistic template fitting. The purpose of this section is to provide a first look at how well these SFRs compare and whether different ways of estimating SFRs give similar answers. An in-depth analysis of MIRI-based SFRs, including new SFR calibrations, will be discussed in Ronayne et al. (2023).

Figure 5 shows how the near-IR and optical emission increases at lower infrared luminosities, indicating that more of the star formation is unobscured. In Figure 10, we compare IR and optical SFRs for our MIRI sample to examine when the two indicators are in disagreement. We calculate the infrared SFRs using the equation

$$\text{SFR } [M_\odot \text{ yr}^{-1}] = 1.59 \times 10^{-10} {}^* L_{IR} \, [L_\odot], \qquad (9)$$

which assumes a Kroupa initial mass function (Kroupa 2001; Murphy et al. 2011).

The optical SFRs come from the CANDELS catalogs of Stefanon et al. (2017), following methods described there (see also Dahlen et al. 2013 and Santini et al. 2015). Briefly, the SFRs are derived by fitting the CANDELS UV/optical photometry in 10 different ways, each fit using a different code, priors, grid sampling, and star formation history. The final value is the median from the different fits. Optical SFRs are sensitive to the photometric redshift of the galaxy. The
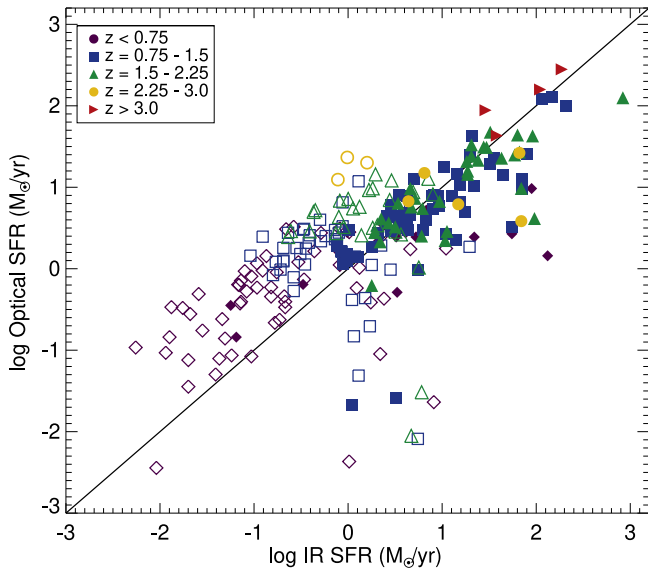
Figure 10. Optical vs. IR SFRs, where symbol color and shape correspond to redshift. Mid-IR weak galaxies are shown as open symbols. At lower luminosities, the bulk of star formation is unobscured, which is reflected by the optical SFRs being systematically higher than the IR SFRs. This is mainly an issue for the mid-IR weak galaxies.

optical SFRs from Stefanon et al. (2017) were computed using photometric redshifts from that catalog, whereas for CEERS MIRI galaxies, we also use photometric redshifts from Finkelstein et al. (2022; see Section 2.2). For this reason, we keep only those sources where the photo-zs from Stefanon et al. (2017) and Finkelstein et al. (2022) agree within $\Delta z < 0.15$. Similarly, we also remove any sources where the MIRI and optical redshifts differ by more than 0.15. The remainder of the sample is shown in Figure 10.

There is generally a one-to-one correlation between the optical and IR SFRs, and there is no trend away from the one-to-one line with increasing $f(AGN)_{MIR}$. The disagreement is strongest for a handful of mid-IR weak galaxies, where the optical SFRs greatly underpredict the IR SFRs. At $L_{IR} < 10^{10} L_\odot$, the optical SFRs are nearly universally higher than the IR SFRs. IR SFRs may underpredict the true SFR at low luminosities, when the bulk of star formation is unobscured. Interestingly, Figure 10 shows that the disagreement between optical and IR SFRs depends on whether a galaxy is classified as mid-IR weak or dust-rich, rather than on luminosity or redshift. For the mid-IR weak galaxies, the optical SFRs are higher, while for the dust-rich galaxies, the IR SFRs are higher. Dust-rich galaxies at the same redshifts or luminosities as mid-IR weak galaxies lie closer to the one-to-one line.

Optical SFRs themselves carry a high degree of uncertainty, as there are many degeneracies that plague this portion of a galaxy's SED, including stellar ages and dust attenuation (Bell 2003; Leja et al. 2019). This comparison between SFR indicators is for optical- and IR-based SFRs calculated with template fitting to a few photometric data points. Roynane et al. (2023, in preparation) compares mid-IR-based SFRs with UV-based SFRs and finds a much stronger agreement. The most accurate estimations of SFRs will likely come from combining either UV or spectroscopic indicators, such as Hα, with mid-IR estimators (Murphy et al. 2011; Kennicutt & Evans 2012).

5. Conclusions

We have examined the demographics of the CEERS MIRI survey, which comprises four pointings in the EGS field covering the F770W–F2100W filters. We summarize our findings below.

1. Comparison with the Spitzer 24 μm population. MIRI sources peak at $z \sim 1.3$ and lack many high-redshift detections seen in the MIPS 24 μm population. This is due both to MIRI's smaller FOV and to MIRI's lower-wavelength filters (which are more sensitive) no longer tracing dust beyond $z > 3$. A large-area MIRI survey will be required to build up a large high-redshift population. However, in much shorter integration times, MIRI probes an order of magnitude fainter than MIPS due to the increased sensitivity of JWST. MIRI is best at identifying galaxies with $L_{IR} < 10^{10} L_\odot$ at cosmic noon ($z = 1$–2).

2. Mid-IR weak galaxies. Until now, with the improved mid-IR coverage and sensitivity of JWST, it was impossible to know exactly what the mid-IR emission of $L_{IR} < 10^{10} L_\odot$ galaxies at cosmic noon looked like. We fit the MIRI and IRAC 4.5 μm photometry with a suite of dusty star-forming templates, AGN templates, and templates created from local low-luminosity galaxies. We find that inclusion of the 4.5 μm data point is essential to discriminate between AGN and mid-IR weak galaxies, as their mid-IR emission can look very similar. It is only by comparing the mid-IR emission with rest-frame near-IR emission that one can distinguish between a mid-IR power law due to an AGN torus and weak mid-IR emission due to an intrinsically low-luminosity galaxy. We find that mid-IR weak galaxies dominate the MIRI population at $L_{IR} < 10^{10} L_\odot$. In these galaxies, the SED is dominated by near-IR emission, indicating that the star formation is predominantly unobscured. For that reason, we recommend that infrared SFRs be used with extreme caution.

3. AGN identification with colors. The AGN fraction increases with L_{IR}, which may reflect an increasing accretion efficiency, or it may reflect the challenges in separating AGN from mid-IR weak galaxies at lower luminosities. Spectroscopic surveys are necessary to distinguish between the two scenarios. We find that AGN can be reliably identified by combining two color selections: S_{1800W}/S_{1000W} versus S_{1280W}/S_{1000W} and $S_{1800W}/S_{3.6}$ versus $S_{1000W}/S_{3.6}$. The 10 μm number counts reveal that AGN are extremely rare (a handful appear in each MIRI pointing), so large-area MIRI surveys are required to build up sufficient samples of mid-IR AGN to study supermassive black hole growth at cosmic noon.

MIRI is revealing many interesting properties of galaxies at cosmic noon, but the JWST results are hampered by its small FOV and lack of longer-wavelength filters. All of the results in this paper will be strengthened with the upcoming MEGA survey (PI: Kirkpatrick; Cycle 2 GO-3794), which will observe the EGS field with an additional 26 MIRI pointings. A new far-IR telescope that matches JWST's sensitivity would also allow for the unambiguous measurement of L_{IR}.

Acknowledgments

ORCID iDs

Allison Kirkpatrick ⓘ https://orcid.org/0000-0002-5537-8110
Guang Yang ⓘ https://orcid.org/0000-0001-8835-7722
Aurélien Le Bail ⓘ https://orcid.org/0000-0002-9466-2763
Eric F. Bell ⓘ https://orcid.org/0000-0002-5564-9873
Nikko J. Cleri ⓘ https://orcid.org/0000-0001-7151-009X
David Elbaz ⓘ https://orcid.org/0000-0002-7631-647X
Steven L. Finkelstein ⓘ https://orcid.org/0000-0001-8519-1130
Nimish P. Hathi ⓘ https://orcid.org/0000-0001-6145-5090
Michaela Hirschmann ⓘ https://orcid.org/0000-0002-3301-3321
Benne W. Holwerda ⓘ https://orcid.org/0000-0002-4884-6756
Dale D. Kocevski ⓘ https://orcid.org/0000-0002-8360-3880
Ray A. Lucas ⓘ https://orcid.org/0000-0003-1581-7825
Jed McKinney ⓘ https://orcid.org/0000-0002-6149-8178
Casey Papovich ⓘ https://orcid.org/0000-0001-7503-8482
Pablo G. Pérez-González ⓘ https://orcid.org/0000-0003-4528-5639
Alexander de la Vega ⓘ https://orcid.org/0000-0002-6219-5558
Micaela B. Bagley ⓘ https://orcid.org/0000-0002-9921-9218
Emanuele Daddi ⓘ https://orcid.org/0000-0002-3331-9590
Mark Dickinson ⓘ https://orcid.org/0000-0001-5414-5131
Henry C. Ferguson ⓘ https://orcid.org/0000-0001-7113-2738
Adriano Fontana ⓘ https://orcid.org/0000-0003-3820-2823
Andrea Grazian ⓘ https://orcid.org/0000-0002-5688-0663
Norman A. Grogin ⓘ https://orcid.org/0000-0001-9440-8872
Pablo Arrabal Haro ⓘ https://orcid.org/0000-0002-7959-8783
Jeyhan S. Kartaltepe ⓘ https://orcid.org/0000-0001-9187-3605
Lisa J. Kewley ⓘ https://orcid.org/0000-0001-8152-3943
Anton M. Koekemoer ⓘ https://orcid.org/0000-0002-6610-2048
Jennifer M. Lotz ⓘ https://orcid.org/0000-0003-3130-5643
Laura Pentericci ⓘ https://orcid.org/0000-0001-8940-6768
Nor Pirzkal ⓘ https://orcid.org/0000-0003-3382-5941
Swara Ravindranath ⓘ https://orcid.org/0000-0002-5269-6527
Rachel S. Somerville ⓘ https://orcid.org/0000-0002-6748-6821
Jonathan R. Trump ⓘ https://orcid.org/0000-0002-1410-0470
Stephen M. Wilkins ⓘ https://orcid.org/0000-0003-3903-6935
L. Y. Aaron. Yung ⓘ https://orcid.org/0000-0003-3466-035X

References

Ananna, T. T., Treister, E., Urry, C. M., et al. 2019, ApJ, 871, 240
Backhaus, B. E., Trump, J. R., Cleri, N. J., et al. 2022, ApJ, 926, 161
Bell, E. F. 2003, ApJ, 586, 794
Bonato, M., Sajina, A., De Zotti, G., et al. 2017, ApJ, 836, 171
Boquien, M., Kennicutt, R., Calzetti, D., et al. 2016, A&A, 591, A6
Brammer, G. B., van Dokkum, P. G., & Coppi, P. 2008, ApJ, 686, 1503
Calzetti, D., Kennicutt, R. C., Engelbracht, C. W., et al. 2007, ApJ, 666, 870
Caputi, K. I., Lagache, G., Yan, L., et al. 2007, ApJ, 660, 97
Chary, R., Casertano, S., Dickinson, M. E., et al. 2004, ApJS, 154, 80
Chary, R., & Elbaz, D. 2001, ApJ, 556, 562
Cleri, N. J., Olivier, G. M., Hutchison, T. A., et al. 2023a, ApJ, 953, 10
Cleri, N. J., Yang, G., Papovich, C., et al. 2023b, ApJ, 948, 112
Cortzen, I., Garrett, J., Magdis, G., et al. 2019, MNRAS, 482, 1618
Dahlen, T., Mobasher, B., Faber, S. M., et al. 2013, ApJ, 775, 93
Dalcanton, J. J., Yoachim, P., & Bernstein, R. A. 2004, ApJ, 608, 189
Dale, D. A., & Helou, G. 2002, ApJ, 576, 159
Del Moro, A., Alexander, D. M., Bauer, F. E., et al. 2016, MNRAS, 456, 2105
Delvecchio, I., Gruppioni, C., Pozzi, F., et al. 2014, MNRAS, 439, 2736
Donley, J. L., Koekemoer, A. M., Brusa, M., et al. 2012, ApJ, 748, 142
Draine, B. T., & Li, A. 2007, ApJ, 657, 810
Elbaz, D., Daddi, E., Le Borgne, D., et al. 2007, A&A, 468, 33
Elbaz, D., Dickinson, M., Hwang, H. S., et al. 2011, A&A, 533, A119
Elitzur, M., Ho, L. C., & Trump, J. R. 2014, MNRAS, 438, 3340
Fazio, G. G., Ashby, M. L. N., Barmby, P., et al. 2004, ApJS, 154, 39
FIDEL Team 2020, Far-Infrared Deep Extragalactic Legacy Survey, IPAC, doi:10.26131/IRSA410
Finkelstein, S. L., Bagley, M., Song, M., et al. 2022, ApJ, 928, 52
Gardner, J. P., Mather, J. C., Clampin, M., et al. 2006, SSRv, 123, 485
Grogin, N. A., Kocevski, D. D., Faber, S. M., et al. 2011, ApJS, 197, 35
Hao, H., Elvis, M., Civano, F., et al. 2010, ApJL, 724, L59
Hatcher, C., Kirkpatrick, A., Fornasini, F., et al. 2021, AJ, 162, 65
Hickox, R. C., & Alexander, D. M. 2018, ARA&A, 56, 625
Holwerda, B. W., Bianchi, S., Böker, T., et al. 2012, A&A, 541, L5
Holwerda, B. W., Keel, W. C., Williams, B., Dalcanton, J. J., & de Jong, R. S. 2009, AJ, 137, 3000
Holwerda, B. W., Wu, J. F., Keel, W. C., et al. 2021, ApJ, 914, 142
Jarrett, T. H., Cohen, M., Masci, F., et al. 2011, ApJ, 735, 112
Jin, S., Daddi, E., Liu, D., et al. 2018, ApJ, 864, 56
Kartaltepe, J. S., Dickinson, M., Alexander, D. M., et al. 2012, ApJ, 757, 23
Kennicutt, R. C., & Evans, N. J. 2012, ARA&A, 50, 531
Kennicutt, R. C., Jr 1998, ApJ, 498, 541
Kirkpatrick, A., Alberts, S., Pope, A., et al. 2017a, ApJ, 849, 111
Kirkpatrick, A., Pope, A., Alexander, D. M., et al. 2012, ApJ, 759, 139
Kirkpatrick, A., Pope, A., Aretxaga, I., et al. 2014, ApJ, 796, 135
Kirkpatrick, A., Pope, A., Charmandaris, V., et al. 2013, ApJ, 763, 123
Kirkpatrick, A., Pope, A., Sajina, A., et al. 2015, ApJ, 814, 9
Kirkpatrick, A., Pope, A., Sajina, A., et al. 2017b, ApJ, 843, 71
Koekemoer, A. M., Faber, S. M., Ferguson, H. C., et al. 2011, ApJS, 197, 36
Kroupa, P. 2001, MNRAS, 322, 231
Lacy, M., Storrie-Lombardi, L. J., Sajina, A., et al. 2004, ApJS, 154, 166
Langeroodi, D., & Hjorth, J. 2023, ApJL, 946, L40
Leja, J., Carnall, A. C., Johnson, B. D., Conroy, C., & Speagle, J. S. 2019, ApJ, 876, 3
Liu, D., Daddi, E., Dickinson, M., et al. 2018, ApJ, 853, 172
Lyu, J., & Rieke, G. 2022, Univ, 8, 304
Lyu, J., Rieke, G. H., & Shi, Y. 2017, ApJ, 835, 257
Magnelli, B., Elbaz, D., Chary, R. R., et al. 2009, A&A, 496, 57
Magnelli, B., Elbaz, D., Chary, R. R., et al. 2011, A&A, 528, A35
Magnelli, B., Gómez-Guijarro, C., Elbaz, D., et al. 2023, A&A, 678, A83
Mason, R. E., Lopez-Rodriguez, E., Packham, C., et al. 2012, AJ, 144, 11
McKinney, J., Pope, A., Armus, L., et al. 2020, ApJ, 892, 119
Merlin, E., Fontana, A., Ferguson, H. C., et al. 2015, A&A, 582, A15
Messias, H., Afonso, J., Salvato, M., Mobasher, B., & Hopkins, A. M. 2012, ApJ, 754, 120
Murphy, E. J., Condon, J. J., Schinnerer, E., et al. 2011, ApJ, 737, 67
Negus, J., Comerford, J. M., Sánchez, F. M., et al. 2023, ApJ, 945, 127
Newman, J. A., & Gruen, D. 2022, ARA&A, 60, 363
Noeske, K. G., Weiner, B. J., Faber, S. M., et al. 2007, ApJL, 660, L43
Padovani, P., Alexander, D. M., Assef, R. J., et al. 2017, A&ARv, 25, 2
Papovich, C., Cole, J., Yang, G., et al. 2023, ApJL, 949, L18
Papovich, C., Dole, H., Egami, E., et al. 2004, ApJS, 154, 70
Peca, A., Cappelluti, N., Urry, C. M., et al. 2023, ApJ, 943, 162
Pérez-González, P. G., Rieke, G. H., Egami, E., et al. 2005, ApJ, 630, 82
Petric, A. O., Armus, L., Howell, J., et al. 2011, ApJ, 730, 28
Pope, A., Chary, R.-R., Alexander, D. M., et al. 2008, ApJ, 675, 1171
Pope, A., Wagg, J., Frayer, D., et al. 2013, ApJ, 772, 92
Rieke, G. H., Alonso-Herrero, A., Weiner, B. J., et al. 2009, ApJ, 692, 556
Rieke, G. H., Wright, G. S., Böker, T., et al. 2015, PASP, 127, 584
Rodighiero, G., Vaccari, M., Franceschini, A., et al. 2010, A&A, 515, A8

Ronayne, K., Papovich, C., Yang, G., et al. 2023, arXiv:2310.07766
Sajina, A., Yan, L., Fadda, D., Dasyra, K., & Huynh, M. 2012, ApJ, 757, 13
Santini, P., Ferguson, H. C., Fontana, A., et al. 2015, ApJ, 801, 97
Schreiber, C., Elbaz, D., Pannella, M., et al. 2018, A&A, 609, A30
Shen, L., Papovich, C., Yang, G., et al. 2023, ApJ, 950, 7
Stefanon, M., Yan, H., Mobasher, B., et al. 2017, ApJS, 229, 32
Stern, D., Eisenhardt, P., Gorjian, V., et al. 2005, ApJ, 631, 163
Stone, M., Pope, A., McKinney, J., et al. 2022, ApJ, 934, 27
Tardugno Poleo, V., Finkelstein, S. L., Leung, G., et al. 2023, AJ, 165, 153

Trewhella, M., Davies, J. I., Alton, P. B., Bianchi, S., & Madore, B. F. 2000, ApJ, 543, 153
Volonteri, M., Reines, A. E., Atek, H., Stark, D. P., & Trebitsch, M. 2017, ApJ, 849, 155
Xilouris, E. M., Madden, S. C., Galliano, F., Vigroux, L., & Sauvage, M. 2004, A&A, 416, 41
Yang, G., Caputi, K. I., Papovich, C., et al. 2023a, ApJL, 950, L5
Yang, G., Papovich, C., Bagley, M., et al. 2023b, ApJL, 956, L12
Yang, G., Papovich, C., Bagley, M. B., et al. 2021, ApJ, 908, 144
Yuan, F., & Narayan, R. 2014, ARA&A, 52, 529